Monthly Notices
of the
ROYAL ASTRONOMICAL SOCIETY

MNRAS **509,** 2736–2757 (2022)
Advance Access publication 2021 November 9
https://doi.org/10.1093/mnras/stab3179

Milankovitch cycles for a circumstellar Earth-analogue within α Centauri-like binaries

B. Quarles ,[1,2]★ G. Li[1] and J. J. Lissauer[3]

[1]*Center for Relativistic Astrophysics, School of Physics, Georgia Institute of Technology, Atlanta, GA 30332, USA*
[2]*Department of Physics, Astronomy, Geosciences and Engineering Technology, Valdosta State University, Valdosta, GA 31698, USA*
[3]*Space Science and Astrobiology Division, MS 245-3, NASA Ames Research Center, Moffett Field, CA 94035, USA*

Accepted 2021 October 29. Received 2021 September 28; in original form 2021 July 23

ABSTRACT

An Earth-analogue orbiting within the habitable zone of α Centauri B was shown to undergo large variations in its obliquity, or axial tilt, which affects the planetary climate by altering the radiative flux for a given latitude. We examine the potential implications of these obliquity variations for climate through Milankovitch cycles using an energy balance model with ice growth and retreat. Similar to previous studies, the largest amplitude obliquity variations from spin-orbit resonances induce snowball states within the habitable zone, while moderate variations can allow for persistent ice caps or an ice belt. Particular outcomes for the global ice distribution can depend on the planetary orbit, obliquity, spin precession, binary orbit, and which star the Earth-analogue orbits. An Earth-analogue with an inclined orbit relative to the binary orbital plane can periodically transition through several global ice distribution states and risk runaway glaciation when ice appears at both poles and the equator. When determining the potential habitability for planets in general stellar binaries, more care must be taken due to the orbital and spin dynamics. For Earth-analogues within the habitable zone of α Centauri B can experience a much greater range of climate states, which is in contrast to Earth-analogues in the habitable zone of α Centauri A.

Key words: planets and satellites: atmospheres – planets and satellites: dynamical evolution and stability – binaries: general – stars: individual: α Centauri.

1 INTRODUCTION

Current surveys of stellar multiplicity indicate that nearly half of Sun-like stars have stellar companions (Raghavan et al. 2010; Moe & Di Stefano 2017). The most recent census of Kepler planets (Bryson et al. 2021) suggests that nearly half of all Sun-like stars harbor an Earth-like planet in its habitable zone (i.e. orbital region where liquid water could potentially exist). As a result, the prospect of planets in binary systems is now more compelling. New observations using direct imaging have uncovered a possible Neptune-sized planet orbiting α Centauri A (Wagner et al. 2021), which is the primary star within the closest stellar system to the Sun (∼4 ly). Future observations using the *James Webb Space Telescope* (*JWST*) will help identify the large planets orbiting α Centauri A (Beichman et al. 2020), which will also have implications for prospective planets orbiting the companion star, α Centauri B. The habitability of planets orbiting either star depends on more factors than those typically used for single star systems (Kasting, Whitmire & Reynolds 1993).

The habitable zone (HZ), as defined for our Solar system, is typically calculated using atmospheric models with a single energy source (Kopparapu et al. 2013a,b, 2014). The HZ definition has expanded to include binary stars (Eggl et al. 2012; Haghighipour & Kaltenegger 2013; Kaltenegger & Haghighipour 2013; Cukier et al. 2019; Eggl, Georgakarakos & Pilat-Lohinger 2020), where the spectral energy distribution of each star must be taken into account when the radiative flux from the secondary star is non-negligible. Forgan (2012) showed the extent of the HZ around α Centuari B is largely constant, despite the radiative influence from α Centuari A. However, planets within either star's HZ would undergo eccentricity (Quarles & Lissauer 2016; Quarles, Lissauer & Kaib 2018) and obliquity oscillations (Quarles, Li & Lissauer 2019) that can affect the long-term climate stability even when the overall extent of the HZ is static. Perturbations on Earth's orbit and spin precession induce so-called Milankovitch cycles (Milankovitch 1941) that modulate the extent and frequency of ice ages. Large-scale changes in the extent of ice coverage on Earth's surface influence the climate energy balance through albedo and associated feedbacks (i.e. Spiegel et al. 2010; Armstrong et al. 2014; Deitrick et al. 2018a).

Forgan (2016) coupled a 1D latitudinal energy balance model (LEBM) to *N*-body integrations and showed that perturbations from the stellar binary drive variations in the mean temperature for an Earth-like planet. For simulations of an Earth-like planet orbiting α Centauri A, the magnitude of variations was ∼5 K over a range of time-scales depending on whether the types of precession (orbital or axial) considered. Forgan (2016) focused on two archetypal systems, but showed that the decoupled approach of considering the astronomical (i.e. orbit and spin) and radiative perturbations separately was broadly acceptable. Later works (Bazsó et al. 2017; Quarles et al. 2018) showed conditions where the maximum planetary eccentricity is non-negligible (e_p ∼0.15) due to the secular forcing. Moreover, Quarles et al. (2019) illustrated large

---

★ E-mail: billylquarles@gmail.com

Published by Oxford University Press on behalf of Royal Astronomical Society

variations in the planetary obliquity, which have broader implications concerning the periodicity of ice ages. Therefore, we revisit the study of Milankovitch cycles for circumstellar planets in binaries using α Centauri as an archetype.

This work focuses the influence of stellar companions on the growth and retreat of ice coverage as commonly associated with Milankovitch cycles, which can also be used as a proxy for habitability. Thus, we use a 1D LEBM similar to Forgan (2016) and forego the more detailed approach employed through a general circulation model (GCM). The α Centauri system is included in our investigation because the two most massive stars form a binary consisting of Sun-like star of disparate luminosity, which allows for a more rich exploration. Quarles et al. (2019) showed conditions that produce large obliquity variations for an Earth-analogue within α Cen B's HZ, while other works (Armstrong et al. 2014; Deitrick et al. 2018a; Shan & Li 2018; Quarles et al. 2020a) have investigated the capture of planets into a Cassini state (i.e. a 1:1 resonance between the spin angle ψ and ascending node Ω; Colombo 1966; Peale 1969; Ward & Hamilton 2004), where such processes can directly affect the extent of Milankovitch cycles.

This paper explores the effects of obliquity variation on the potential for Milankovitch cycles when an Earth-analogue orbits one star within a stellar binary. Section 2 details our initial conditions and physical processes implemented in the numerical simulations. The influence of obliquity variation on the globally averaged surface temperature, albedo, ice fraction, and ice distribution are discussed in Sections 3 and 4 for an Earth-analogue orbiting either star in α Centauri AB. A broader study is performed in Section 5 for Earth-like planets orbiting the secondary star of a binary that is α Centuari-like with respect to the stellar mass and luminosity, but the binary orbit varies over a range in binary semimajor axis and eccentricity. The main results of our study are summarized in Section 6, along with a comparison to previous results.

2 NUMERICAL METHODS

2.1 Orbital evolution

Many studies (Wiegert & Holman 1997; Holman & Wiegert 1999; Quarles & Lissauer 2016, 2018; Quarles et al. 2018, 2020b) investigated the stability of planets in binaries, including α Centauri AB, and concluded that planetary orbits within the HZ are generally stable, particularly those with low eccentricity ($\lesssim 0.2$) and inclination ($\lesssim 40^\circ$) relative to the binary orbit. As a result, we use the `whfast` integrator with REBOUND (Rein & Liu 2012; Rein & Spiegel 2015) to evolve each system. The time-step for the integrator is set to 5 per cent of the planetary period, which is adequate to keep the numerical errors and simulation wall time low.

Observations of α Centauri AB have improved over time, and we use parameters from Pourbaix & Boffin (2016). The stellar masses are 1.133 (star A) and 0.972 $M_\odot$ (star B), where the orbital parameters are 23.78 AU, 0.524, $77\overset{\circ}{.}05$, and $209\overset{\circ}{.}6901$ for the initial binary semimajor axis $a_{\rm bin}$, eccentricity $e_{\rm bin}$, argument of periastron $\omega_{\rm bin}$, and mean anomaly $MA_{\rm bin}$, respectively. The stellar luminosities are 1.519 (star A) and 0.5 $L_\odot$ (star B), which will be used to scale the planetary orbits within the climate model. For Earth-analogues orbiting either star in α Cen AB, the planetary orbit begins with a semimajor axis $a_{\rm p}$ (in AU) so that the planet receives an Earth-equivalent amount of radiative flux $S(= S_\oplus)$ at the top of its atmosphere through the relation, $a_{\rm p} = \sqrt{L/S}$, using the luminosity in solar units $L_\odot$. The stellar pericentre distance is $\sim$11 AU and the radiative flux for a planet orbiting star B can increase up to 1.3 per cent at conjunction, while the increase is smaller (0.5 per cent) for an Earth-analogue orbiting star A (Quarles & Lissauer 2016). The flux contribution from the stellar companion near its pericentre in either case is significant only at conjunctions and the magnitude of the contribution is much less than the increased flux from the host star at the planet's pericentre. Therefore, we ignore the flux contribution of the stellar companion and focus on its gravitational influence. Additionally, the planetary orbit is apsidally aligned with the binary (i.e. $\omega_{\rm p} = \omega_{\rm bin}$) and near the forced eccentricity (see Quarles et al. 2018). We note that there are stable orbital solutions without our condition of apsidal alignment that result in eccentricity oscillations. We focus on the apsidally aligned case, where the obliquity variations will dominate over the eccentricity variations in the climate model, to reduce the complexity of results. Although, recent planet formation models in binary systems (e.g. Martin, Lissauer & Quarles 2020; Silsbee & Rafikov 2021) showed that discs with apsidal alignment favour conditions for successful planetesimal growth. For planetary orbits around either star, the initial planetary mean anomaly is $222\overset{\circ}{.}492\,236$. All of our results will be averaged over a planetary orbit, which removes any dependence of the planetary mean anomaly. Our previous work (Quarles et al. 2019) explored a range of mutual planetary inclinations in detail, where we restrict this study to include planetary orbits tilted by 2°, 10°, and 30°.

Most of our simulations are evaluated for 0.5 Myr, which captures many secular cycles of the planetary orbit in response to the binary companion. But, we also perform a second set of simulations studying general stellar binaries beyond α Centauri AB. We set the binary semimajor axis ranges from 10 to 90 AU (in 1-AU steps) and eccentricity ranges from 0.0 to 0.9 (in 0.01 steps). In these simulations, the planet orbits star B with an inclination of 10°. Due to spin-orbit resonances, the time-scale for planetary obliquity oscillations can reach 1 Myr and thus, we evolve these cases up to 2 Myr to account for the longer secular time-scale.

2.2 Obliquity evolution

The torque of the host star on the planet's quadrupole moment induces a spin precession on the Earth-analogue, which we account for using the parameter γ[1] in arcsec yr^{-1}. Values for γ are proportional to the square of the planetary rotation rate and the planetary J_2. Previous works (Barnes et al. 2016; Quarles et al. 2020a) used an algorithm from Lissauer, Barnes & Chambers (2012) to calculate the planetary J_2 from the planetary rotation period. We use a similar procedure and produce a table of J_2 values and planetary periods that correspond to our prescribed γ. For each star in α Cen AB, we evaluate a grid of initial spin states with γ ranging from 0 to 100 arcsec yr^{-1} and prograde planetary obliquity $\varepsilon_{\rm o}$ from 0° to 90°. We focus our study on prograde rotation because our previous studies (Barnes et al. 2016; Quarles et al. 2019, 2020a) showed that the positive spin precession frequencies for retrograde are very low amplitude and require a moderate–large planetary eccentricity ($e_{\rm p} \gtrsim 0.3$) to become relevant (Kreyche et al. 2020). Some initial obliquities ($\varepsilon_{\rm o} \sim 89^\circ$) can evolve into the retrograde regime ($\varepsilon > 90^\circ$), for a limited time, where the maximum obliquity is less than 93°. The planetary spin vector is defined by two angles: obliquity ε and spin longitude ψ, where Quarles et al. (2019) explored how the resulting obliquity variation $\Delta\varepsilon$ changes when ψ is chosen randomly. Namely, the $\Delta\varepsilon$

---

[1] This parameter is changed from the conventional α for the precession constant to clearly distinguish with the α used for albedo in the climate model.

can be reduced for instances of strong spin-orbit coupling, but not expanded. Thus, we use a single value for the initial spin longitude ($\psi_{\rm o} = 23\overset{\circ}{.}76$) in all of our simulations.

From these initial parameters, we evolve the secular time-dependant Hamiltonian that includes the canonical variable χ ($=\cos\varepsilon$) and spin longitude ψ in the following equations of motion (Neron de Surgy & Laskar 1997; Saillenfest, Laskar & Boué 2019):

$$\frac{\delta\psi}{\delta t} = \frac{\gamma\chi}{\left(1-e^2\right)^{3/2}} - \frac{\chi}{\sqrt{1-\chi^2}}\left[\mathcal{A}(t)\sin\psi + \mathcal{B}(t)\cos\psi\right] - 2\mathcal{C}(t) \tag{1}$$

$$\frac{\delta\chi}{\delta t} = \sqrt{1-\chi^2}\left[\mathcal{B}(t)\sin\psi - \mathcal{A}(t)\cos\psi\right], \tag{2}$$

where the functions $\mathcal{A}(t)$, $\mathcal{B}(t)$, and $\mathcal{C}(t)$ depend on the orbital evolution of the planet through $p = \sin(i/2)\sin\Omega$ and $q = \sin(i/2)\cos\Omega$ in the following relations:[2]

$$\mathcal{A}(t) = 2\left(\dot{q} + p\left(q\dot{p} - p\dot{q}\right)\right)/\sqrt{1-p^2-q^2}, \tag{3}$$

$$\mathcal{B}(t) = 2\left(\dot{p} - q\left(q\dot{p} - p\dot{q}\right)\right)/\sqrt{1-p^2-q^2}, \tag{4}$$

$$\mathcal{C}(t) = \left(q\dot{p} - p\dot{q}\right), \tag{5}$$

using the numerical integration routines from the SCIPY library (Virtanen et al. 2020) within PYTHON in decade steps between each state that is recorded from a given n-body simulation. In cases where the secular time-scale is shorter than 10 000 yr, the steps are shortened to 5 yr to ensure that changes in obliquity between output steps remain small ($\lesssim 0\overset{\circ}{.}25$).

2.3 Climate model

The most robust method for climate modeling is using a GCM, but such a method is computationally expensive (Way & Georgakarakos 2017) and, consequently, is not amenable to covering large swathes of parameter space. Therefore, we employ a one-dimensional (1D) energy balance model (EBM) that incorporates distinctions between the heat capacities of land masses and oceans. Specifically, we use a modified version of `VPLanet`[3] (Barnes et al. 2020) that directs the `POISE` module (Deitrick et al. 2018b) to read from a file for the orbital and obliquity evolution described in Sections 2.1 and 2.2. To ensure the accuracy within our climate models, the orbital and obliquity evolution is sampled at either 5- or 10-yr intervals. The shorter 5-yr interval is used for special cases when the secular evolution time-scale is sufficiently fast (<10 000 yr), whereas the longer 10-yr interval is used in all other cases. The `POISE` module makes some simplifying assumptions where the planet rotation time-scale is much shorter than the orbital period. Those assumptions are valid for a spin precession constant $\gamma \gtrsim 1\,{\rm arcsec\,yr^{-1}}$ because the orbital period of Earth-like planets in either HZ of α Centauri AB is more than 220 d.

The module `POISE` implements a one-dimensional EBM (Budyko 1969; Sellers 1969) based on North & Coakley (1979) with several modifications specifically including ice coverage evolution (growth, melting, and flow). Additionally, the module divides each latitudinal cell into land and ocean portions to produce a coupled set of equations to model the heat flow. The equations for land and water depend on the parametrized latitude $x = \sin\phi$, where ϕ is the latitude, and are as follows:

$$\begin{aligned} & C_{\rm L}\frac{\partial T_{\rm L}}{\partial t} - D\frac{\partial}{\partial x}\left(1-x^2\right)\frac{\partial T_{\rm L}}{\partial x} + \frac{\nu}{f_{\rm L}}\left(T_{\rm L} - T_{\rm W}\right) + I(x, T_{\rm L}, t) \\ & \quad = S(x,t)\left(1 - \alpha(x, T_{\rm L}, t)\right), \end{aligned} \tag{6}$$

$$\begin{aligned} & m_{\rm d}C_{\rm W}\frac{\partial T_{\rm W}}{\partial t} - D\frac{\partial}{\partial x}\left(1-x^2\right)\frac{\partial T_{\rm W}}{\partial x} + \frac{\nu}{f_{\rm W}}\left(T_{\rm W} - T_{\rm L}\right) + I(x, T_{\rm W}, t) \\ & \quad = S(x,t)\left(1 - \alpha(x, T_{\rm W}, t)\right), \end{aligned} \tag{7}$$

where the latitudinal temperature T and heat capacity C have subscripts corresponding to the land (L) or water (W) portion. Equation (7) contains an adjustable parameter $m_{\rm d}$ that corresponds to the mixing depth within the oceans. These equations describe a balance of energy flow ($C[\partial T/\partial t]$) with the outgoing longwave radiation $I(x, T, t)$, the incident insolation $S(x, t)$, and the planetary albedo α. There is an additional term that contains a parameter ν, the latitudinal temperatures ($T_{\rm L}$ and $T_{\rm W}$), and the fraction f due to land or water. This term is used as a boundary condition within a latitudinal cell and the parameter ν adjusts the land-ocean heat transfer to reasonable values. The total number of latitudinal cells $n_{\rm lat}$ is 151 ranging from –83.4°S to 83.4°N, where the equal steps are taken in the parametrized latitude x. Note that latitude cells of size dx do not have equal width in latitude, but are equal in area (Barnes et al. 2020).

The incident insolation $S(x, t)$ relates to the latitude through the parameter $x = \sin\phi$ and time (or true longitude λ) through the declination $\delta = \psi\sin\lambda$ of the host star. The true longitude marks the location of the planet within its orbit and can be easily calculated (Brouwer & Clemence 1961; Berger 1978) as long as changes to the semimajor axis and eccentricity are small over a single orbit. The magnitude of the insolation $S_\star$ depends on the distance r between the planet and its host star at each point within its orbit, where it is maximal and minimal during the planet's pericentre and apocentre passage, respectively. The general form of $S(x, t)$ is

$$S(x,t) = \frac{L_\star}{4\pi^2 r^2}\left(H_{\rm o}x\sin\delta + \left(1-x^2\right)\cos\delta\sin H_{\rm o}\right), \tag{8}$$

which includes the stellar luminosity $L_\star$ and the hour angle $H_{\rm o}$. The hour angle calculation determines the day length for a given latitude, where many studies have provided derivations (Laskar, Joutel & Boudin 1993; Armstrong et al. 2014; Quarles et al. 2020a) and a detailed discussion is given in the documentation for `VPLanet` (Barnes et al. 2020).

The planetary albedo is separated by surface type (land or water), temperature, and zenith angle. Once the temperature drops below a critical value, then ice forms over the land or water and increases its albedo. As a result, the planetary albedo (see Table 1) is explicitly defined for land grid cells as

$$\alpha = \begin{cases} \alpha_{\rm L} + 0.08P_2(\sin Z), & \text{if } M_{\rm ice} = 0 \text{ and } T_{\rm L} > -2^\circ{\rm C} \\ \alpha_{\rm ice}, & \text{if } M_{\rm ice} > 0 \text{ or } T_{\rm L} \leq -2^\circ{\rm C} \end{cases}, \tag{9}$$

while for water grid cells, it is

$$\alpha = \begin{cases} \alpha_{\rm W} + 0.08P_2(\sin Z), & \text{if } T_{\rm W} > -2^\circ{\rm C} \\ \alpha_{\rm ice}, & \text{if } T_{\rm L} \leq -2^\circ{\rm C} \end{cases}. \tag{10}$$

Shields et al. (2013) showed how the host star's spectral type can affect potential climates through the ice-albedo feedback for FGKM stars, where Earth-analogues orbiting G or K dwarfs exhibit similar feedbacks. However, Wilhelm et al. (2021) showed that the orbital period within the HZ is a bigger effect, which confirms

---

[2] Note that Quarles et al. (2019) contain a typographical error in $\mathcal{B}(t)$, which has been corrected here.

[3] Our modifications to the `POISE` module are included in the current version of the `VPLanet` repository (https://github.com/VirtualPlanetaryLaboratory/vplanet).

Table 1. Parameters for the EBM and ice model in `VPLanet`.

Variable	Value	Units
C_L	1.55×10^7	$J\ m^{-2}\ K^{-1}$
C_W	4.428×10^6	$J\ m^{-3}\ K^{-1}$
m_d	70	m
D	0.58	$W\ m^{-2}\ K^{-1}$
ν	0.8	–
A	203.3	$W\ m^{-2}$
B	2.09	$W\ m^{-2}\ K^{-1}$
α_L	0.363	–
α_W	0.263	–
α_{ice}	0.6	–
f_L	0.34	–
f_W	0.66	–
T_{freeze}	273.15	K
L_h	3.34×10^5	$J\ kg^{-1}$
r_{snow}	2.25×10^{-5}	$kg\ m^{-2}\ s^{-1}$
n_{lat}	151	–

Milankovitch's hypothesis that inter-annual ice coverage depends most strongly on the strength and duration of summer melting. These simulations assume an Earth-analogue planet in the HZ of either α Cen A or α Cen B, where specifically the atmospheric chemical composition ($N_2/H_2O/CO_2$) and the land/water fraction (25 per cent land and 75 per cent water) is nearly identical to Earth values. The land/water fraction is constant across latitudes, where the effect of geography is beyond the scope of this work. Thus, we use the linear parametrized outgoing longwave radiation function,

$$I = A + BT, \tag{11}$$

which is implemented in `VPLanet`, and depends upon the surface temperature T, where values for Earth are adopted from North & Coakley (1979): $A = 203.2$ W m^{-2} and $B = 2.09$ W m^{-2} °C^{-1}.

We are primarily interested in the extent of ice coverage through Milankovitch cycles because of the interplay between ice-albedo feedback with obliquity variations. `VPLanet` models the ice accumulation and ablation in a fashion similar to Armstrong et al. (2014) using the surface temperature T and freezing temperature T_{freeze}, according to the formula in Deitrick et al. (2018b):

$$\frac{dM_{ice}}{dt} = \frac{2.3\sigma}{L_h}\left[T_{freeze}^4 - (T + T_{freeze})^4\right], \tag{12}$$

where M_{ice} is the surface mass density of ice, $\sigma = 5.67 \times 10^{-8}$ W m^{-2} K^{-4} is the Stefan–Boltzmann constant, L_h is the latent heat of fusion of ice, 3.34×10^5 J kg^{-1}, and $T_{freeze} = 273.15$ K. The factor of 2.3 in equation (12) is used to scale the melt rate to roughly Earth values of 3 mm °C^{-1} d^{-1}. Once the land temperature is below freezing, then ice accumulates on land at a constant rate r_{snow}. `VPLanet` allows for modeling of ice flows that modify the height of the ice and bedrock depression, but these effects are beyond the scope of this work. The input parameters used for `VPLanet` are summarized in Table 1. All of our climate simulations begin with an ice-free planet.

3 AN EARTH-ANALOGUE ORBITING α CENTAURI A

The orbital and spin evolution of an Earth-analogue orbiting either star in α Cen AB differs due to the planetary semimajor axis corresponding to the inner edge of the host star's HZ and the mass of the planet-hosting star. In this section, the investigation focuses on a planet orbiting α Cen A inclined by 10° (relative to the binary orbital plane) at its forced eccentricity and holds the initial planetary orbit constant between simulations, while exploring a range of configurations for the initial spin state with respect to the precession constant γ and initial obliquity ε_o. Section 4 explores a similar parameter space, but expands the our study to include three values for the planetary inclination relative to the binary orbital plane.

3.1 Factors affecting Milankovitch cycles

The planetary orbit in our simulations begins at the forced eccentricity ($e_F \approx 0.04$), which warms and cools the whole planet over an orbit (~1.2 yr); however, this short period variation largely averages out over time-scales relevant for global climate. Moreover, starting at the forced eccentricity minimizes variations in the osculating eccentricity (Quarles et al. 2018). Fig. 1 illustrates the evolution in the planetary eccentricity e, obliquity ε, global temperature, global ice fraction f_{ice}, and the global albedo α for two simulations with Earth-like parameters but with different rotation periods (~24 (black) and ~14 h (red)). Fig. 1(a) shows a maximum eccentricity variation $\Delta e \approx 0.008$ over 500 kyr and applies to all of our simulations in Section 3.

A planet representing a modern, moonless Earth has a precession constant of 10 arcsec yr^{-1} (black) in Fig. 1, which results in quite rapid variations in the planetary obliquity $\Delta\varepsilon \sim 22°$ (Fig. 1b). If the planet has a precession constant of 85 arcsec yr^{-1} (red; Fig. 1b), the obliquity variation is reduced to $\Delta\varepsilon \sim 18°$. This reduction is a result of a stronger spin-orbit coupling where the spin precession more closely matches the orbital precession as described in Quarles et al. (2019). The effect of the spin-orbit coupling manifests in the global surface temperature (Fig. 1c) through the frequency of the temperature variations, where the rapid rotator (red) has a lower frequency than the slower rotator (black). Note that the global surface temperature is calculated as a weighted average over the latitude. In addition to a difference in frequency, the slower rotator (black) undergoes larger variations (~3.5°C) in the global mean surface temperature compared to the faster rotator (~1.9°C). The larger oscillation in surface temperature is caused (in part) by the more extreme obliquity variation, where the growth of ice coverage, the excursion to low obliquity ($\varepsilon < 10°$), and changes in albedo all contribute to a higher variation in the global surface temperature. `POISE` is initialized to a steady state temperature, but Fig. 1(c) shows that it is only a local equilibrium because of the ice growth (Figs 1d and e). In general, the growth of ice coverage increase the surface albedo, which causes a decrease in the surface temperature. Such a trend is shown in Figs 1(c)–(e) for the first ~100 kyr until a steady state is achieved in the global ice fraction. Consequently, we ignore the first 100 kyr when computing the variations Δ in our analysis of the full range of initial planetary spin states (i.e. varying γ and ε_o).

Previous works (e.g. Armstrong et al. 2014; Deitrick et al. 2018b) used a parameter that combines the effect of the planetary eccentricity, obliquity, and their associated angles (longitude of pericentre ϖ_p and spin longitude ψ), which is dubbed the Climate Obliquity Precession Parameter (COPP, $e_p\sin(\varepsilon)\sin(\varpi_p + \psi)$). Fig. 2 illustrates the COPP (Fig. 2c) for the modern, moonless Earth-analogue with a spin precession constant set to 10 arcsec yr^{-1} (black curves in Fig. 1) along with the surface temperature (Fig. 2d) and ice mass (Fig. 2e) relative to a given latitude in the Northern hemisphere. The COPP is bounded by the planet's eccentricity and obliquity, while retaining an imprint of both variations, but there is a longer

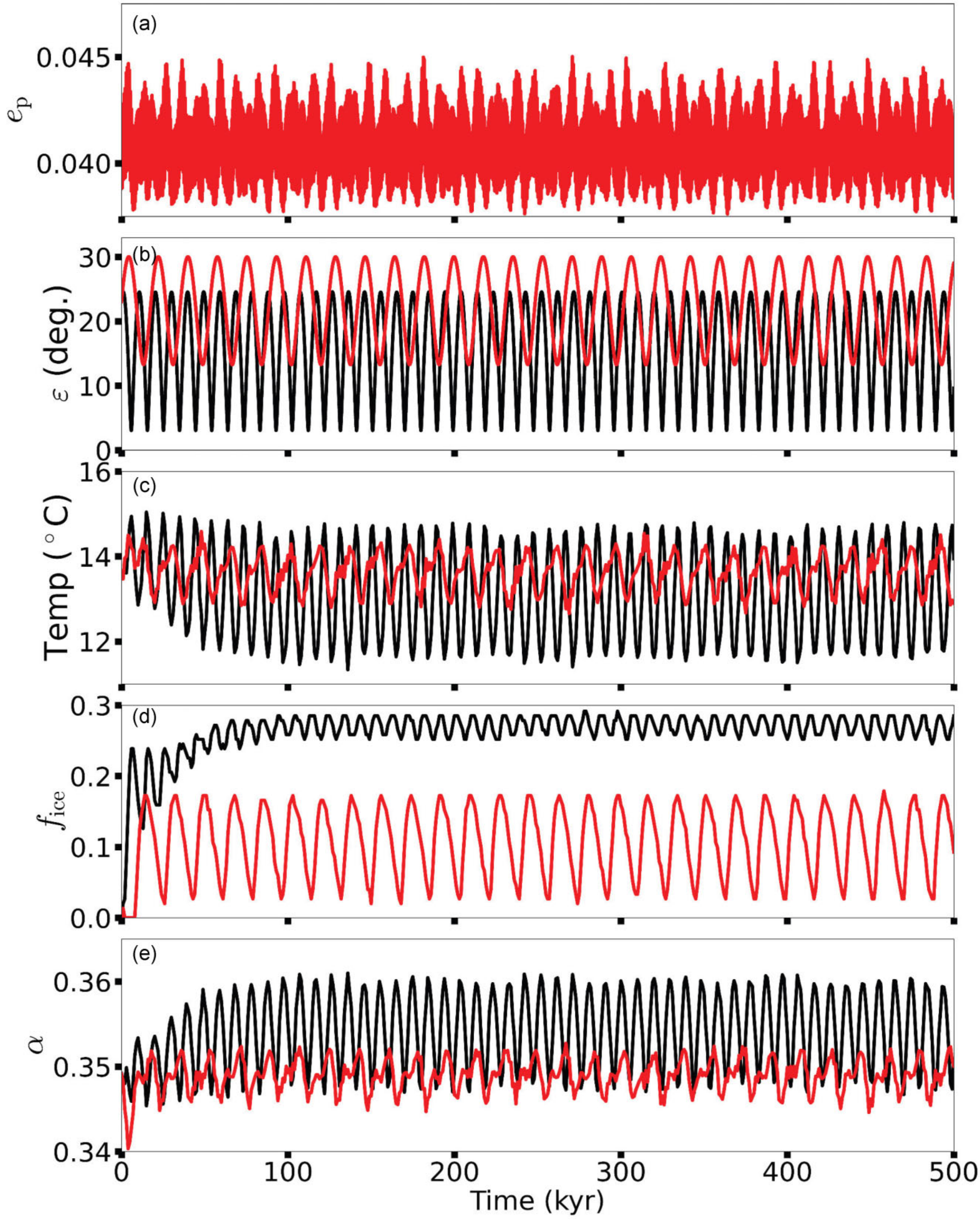

Figure 1. Evolution over a 500-kyr time-scale of the (panel a) planetary eccentricity e_p, (panel b) obliquity ε, (panel c) global surface temperature, (panel d) global ice fraction f_{ice}, and (panel e) global albedo α. The planetary orbit begins near its forced eccentricity at the inner edge of α Cen A's HZ with an inclination of 10°. The initial planetary obliquity ε is similar to modern Earth obliquity (23°), where the precession constant γ is either 10 (black) or 85 arcsec yr^{-1} (red). The former precession constant represents a modern, moonless Earth ($P_{rot} \sim 24$ h) and the latter represents a more rapidly spinning Earth ($P_{rot} \sim 14$ h). The planetary orbit between these simulations is identical and thus, the evolution for the eccentricity overlaps exactly.

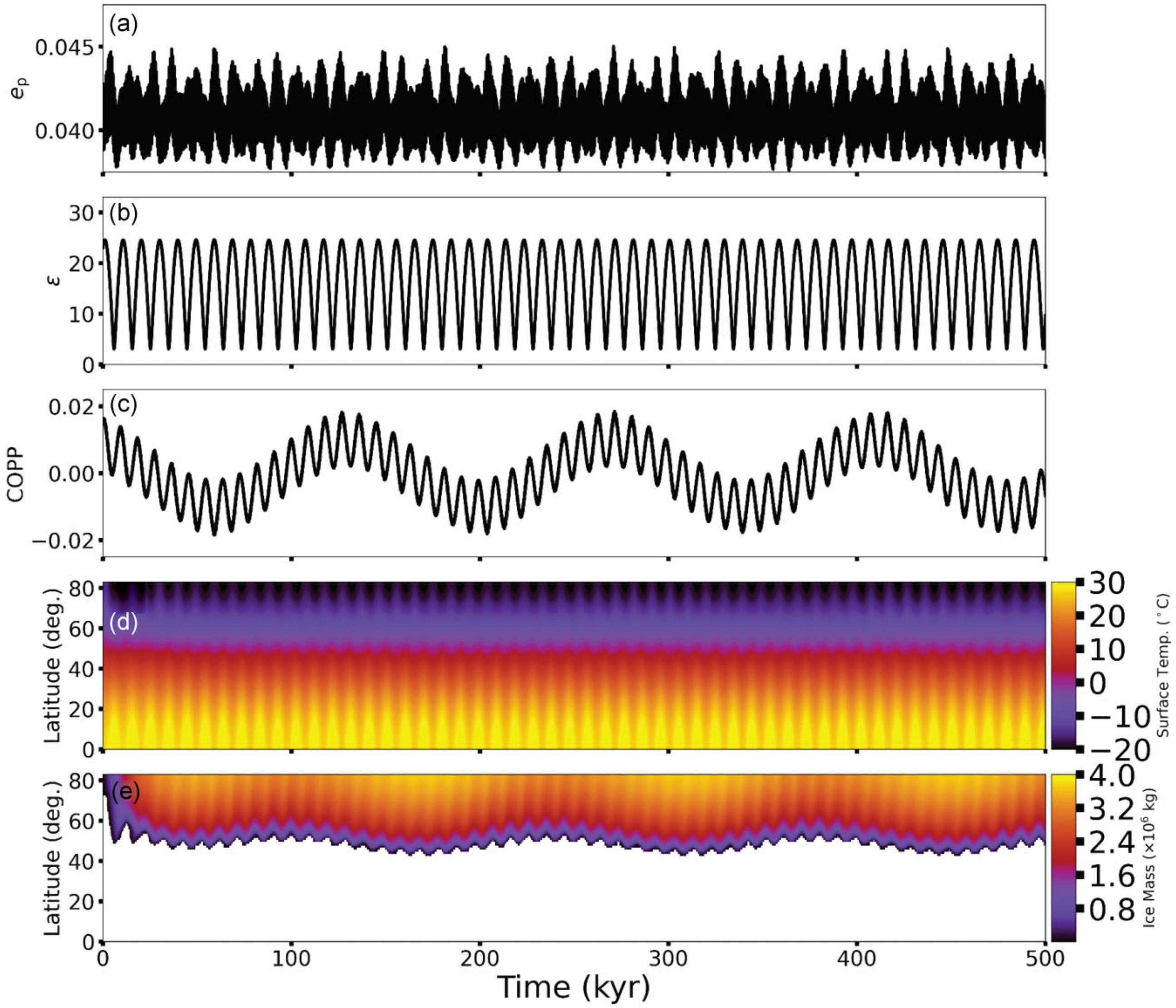

Figure 2. Simulation for 500 kyr of an Earth-analogue ($\varepsilon = 23^\circ$) orbiting α Cen A with a spin precession constant equal to 10 arcsec yr^{-1} showing the evolution in the (panel a) planetary eccentricity $e_{\rm p}$, (panel b) obliquity ε, (panel c) COPP ($e_{\rm p}\sin(\varepsilon)\sin(\varpi_{\rm p} + \psi)$), (panel d) latitudinal surface temperature, and (panel e) latitudinal ice mass. The white cells in panel (e) represent latitudes with very little ice accumulation ($<10^4$ kg) or 'ice-free'.

($\sim$140 kyr) cycle from the combination of orbital and spin precession. Milankovitch cycles for the Earth arise from the combination of the short and long time-scales from the spin and orbital precession. Similar trends occur within our numerical simulation for a planet orbiting α Cen A as shown by the light/dark variations for the surface temperature and ice mass in Figs 2(d) and (e), respectively. The white cells in Fig. 2(e) mark latitudes with very little ice mass ($<10^4$ kg) that we categorize as 'ice-free' because the transition from no ice to significant ice coverage is stark, partly due to our limited resolution in latitude.

To disentangle the contribution of orbital or spin precession, we produce a similar analysis, but for a larger spin precession constant (85 arcsec yr^{-1}) in Fig. 3. The orbital evolution between the two cases (Figs 2 and 3) is identical and thus the changes to the COPP (Fig. 3c) are largely due to the higher spin precession. The Milankovitch cycles are more dramatic, where the higher latitudes undergo enough warming for the ice coverage to periodically retreat by $\sim$15° poleward in latitude.

3.2 Obliquity and global surface temperature variations

For a broader view, we perform simulations considering a prograde rotating planet ($\varepsilon = 0^\circ$–90°) and a wide range of precession constants ($\gamma = 0$–100 arcsec yr^{-1}) in Fig. 4, where the variations of each parameter are colour-coded. We note that the maximum obliquity does not exceed 90° in any of our simulations and the obliquity range when $\varepsilon_{\rm o} \sim 90^\circ$ extends to lower obliquity. The white ⊕ symbol denotes initial conditions for a modern, moonless Earth-analogue ($\gamma = 10$ arcsec yr^{-1} and $\varepsilon_{\rm o} = 23^\circ$). For all of these simulations, the planet begins at the inner edge of α Cen A's HZ so that the planet receives an Earth-equivalent amount of radiative flux at the top of its atmosphere and the planetary orbit begins inclined 10° relative to the binary orbital plane, where we expect an obliquity variation $\Delta\varepsilon \approx 15^\circ$–$20^\circ$ from the induced nodal precession on the planetary orbit. This explains much of the parameter space (light green regions) in Fig. 4(a).

Stronger spin-orbit coupling produces a strip of lower than expected obliquity variation (yellow) similar to the case for α Cen

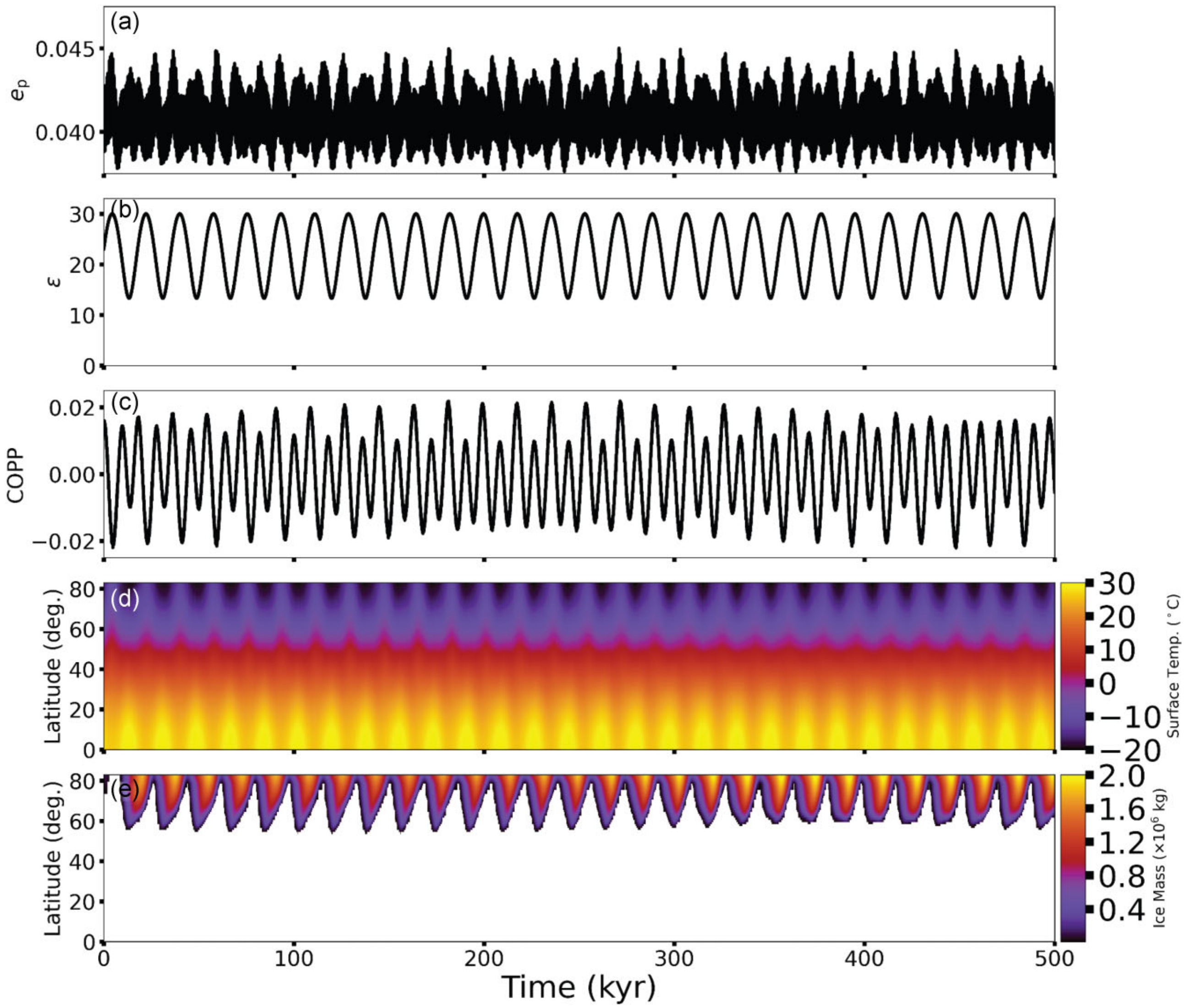

Figure 3. Similar to Fig. 2, but for an Earth-analogue with a spin precession constant equal to 85 arcsec yr^{-1}.

B (Quarles et al. 2019), corresponding to the region close to the Cassini state. The wide separation of secular modes within α Cen A's HZ prevent the large obliquity variations seen for fast rotators ($\gamma \sim$ 80–100 arcsec yr^{-1}) in α Cen B's HZ examined in Quarles et al. (2019). The relatively mild obliquity variation for an Earth-analogue orbiting α Cen A correlates with a mild variation (ΔT) in the global surface temperature with a maximum of 5.6°C in Fig. 4(b). The strip of lower obliquity variation also induces some of the smallest surface temperature variations for low initial obliquity. Intermediate values of initial obliquity (30°–50°) exhibit the maximum surface temperature variation, while the highest obliquities have much lower ΔT.

3.3 Ice fraction and surface distribution

Two strongly correlated factors that affect a planet's global surface temperature, and thereby its habitability, are the global ice fraction ($\Delta f_{\rm ice}$) and albedo ($\Delta \alpha$) variations. Our simulations begin completely ice-free, where a dynamic equilibrium in ice coverage is established within ∼100 kyr. Our calculations of the variation exclude the first 100 kyr to remove this bias and so we can measure the overall variation relative a steady state. Figs 4(c) and (d) show their highest variations are correlated with the global surface temperature (Fig. 4b). The largest variation in global ice fraction is ∼0.2–0.3, resulting in a variation in the global albedo of ∼0.03. There is also a similar trend with respect to the initial obliquity as seen in the surface temperature variation. The global variation provides a broad overview, but is insufficient in the necessary details for Milankovitch cycles.

From our simulations, we categorize the ice distribution into four states: (1) ice-free, (2) ice caps, (3) ice belt, and (4) snowball, where each of these are determined after the removal of the first 100 kyr. The ice-free category describes planets where ice does not accumulate year to year, although seasonal ice is still possible. It is possible that ice accumulates and ablates between the 1000-yr interval for our simulation outputs, but we consider this scenario fine-tuned and unlikely. The snowball category designates when ice coverage grows to cover the entire planet, which persists throughout the simulation. There are additional options available in `POISE` (e.g. more sophisticated heat diffusion or CO_2 partial pressures) that could allow for snowballs to thaw, but this is beyond the scope of this work. Ice caps or ice belt are states with ice that extend

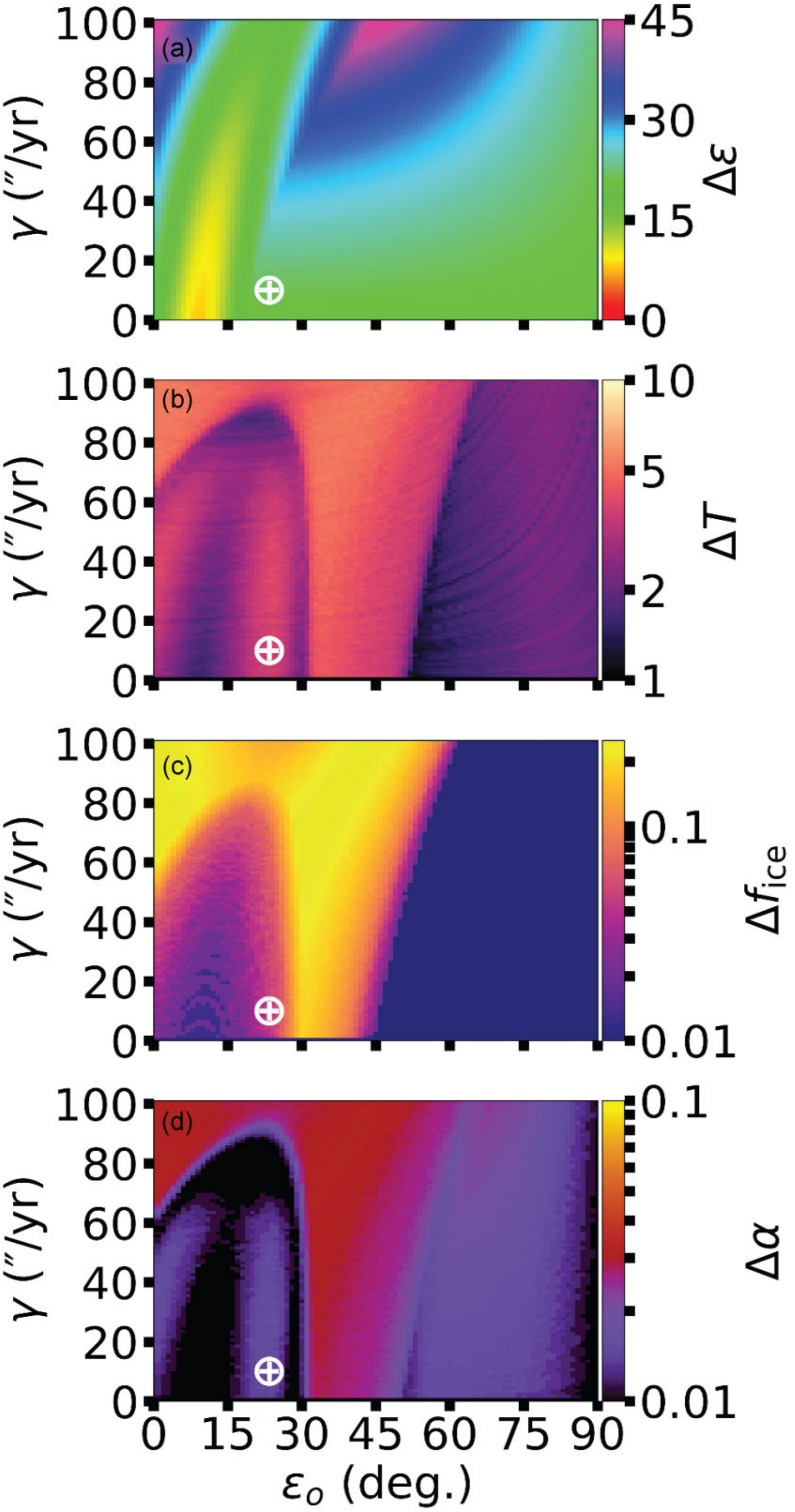

Figure 4. The variation of the (panel a) obliquity $\Delta\varepsilon$, (panel b) global surface temperature ΔT, (panel c) global ice fraction $\Delta f_{\rm ice}$, and (panel d) global albedo $\Delta\alpha$ using simulations with an EBM over 400 kyr for an Earth-analogue orbiting α Cen A, where the planet's orbit is initially inclined by 10° relative to the binary orbit. The initial spin is varied with respect to the spin precession constant γ and the initial obliquity $\varepsilon_{\rm o}$. The white $\oplus$ symbol designates conditions ($\varepsilon_{\rm o} = 23^\circ$, $\gamma = 10\,{\rm arcsec\,yr^{-1}}$, $P_{\rm rot} \sim 24$ h) for a modern, moonless Earth.

from the pole down to 30° N or from the equator up to 30° N (Williams & Pollard 2003; Rose, Cronin & Bitz 2017), respectively. Since the planetary eccentricity in our simulations remains nearly circular, the ice distributions are largely symmetric relative to the equator. Armstrong et al. (2014) showed that this is not the case for highly inclined and eccentric planets, where more sophisticated categorization criteria than what we employ would be required in those circumstances (e.g. orbits closer to the binary mean motion resonances). Our model does permit transitions between the ice-free, ice caps, and ice belt states, which is the essence of Earth-like Milankovitch cycles. The Earth science community will refer to an *ice cap* by the extent of ice coverage on land (i.e. less than 50 000 km^2). Our usage of ice cap is different, where ice caps are states with ice that extends from the pole to at least 30°, without a delineation between land/ocean coverage.

Fig. 5 illustrates our results in Fig. 5(a) using the ice distribution categorization scheme in addition to the maximum (Fig. 5b) and minimum (Fig. 5c) global ice fraction. The ice distributions in Fig. 5(a) are colour-coded, where the magenta hatched region denotes simulations where the planet oscillates between an ice-free state and one with polar ice caps. The ice belt and snowball categories are present for consistency with a similar figure (Fig. 12), although these categories were not observed for any of the simulations for α Cen A. The white $\oplus$ symbol denotes initial conditions representing a modern, moonless Earth as previously indicated in Fig. 4. Fig. 5(a) shows two states (ice-free or ice caps), where permanent ice caps (solid grey) are possible for low obliquities and a broad range in spin precession constant. Surrounding this region (magenta hatches), ice caps persist most of the time and interrupted by relatively brief ice-free periods. This can also be deduced (to some degree) from spotting the differences between Figs 5(b) and (c), which indicate the respective maximum and minimum global ice fraction attained over a simulation or using the global ice fraction variation in Fig. 4(c). Alternatively, there are scenarios when the polar caps state is transient and an ice-free state is more common, which is indicated by the magenta hatching on the black background in Fig. 5(a). In this regime, the ice fraction strongly depends on the initial obliquity and more weakly depends on the spin precession constant. For $\epsilon_o > 60°$, each model produce an ice-free planet, which is due to the weak planetary spin-orbit coupling that induces up to a 20° variation in obliquity on an ∼10 000-yr time-scale (i.e. secular orbital eccentricity variations). One might expect an ice belt to form if a planet begins at high obliquity (Williams & Pollard 2003; Rose et al. 2017; Kilic et al. 2018), but the planet's obliquity evolves quickly (within ∼5000 yr) to lower values such that the ice ablation rate matches the accumulation and no significant growth in ice coverage can occur.

4 AN EARTH-ANALOGUE ORBITING α CENTAURI B

An Earth-analogue orbiting α Cen B can experience similar outcomes to those discussed in the Section 3 due to the approximate mass symmetry of the host binary. However, α Cen B is less luminous than α Cen A, which places α Cen B's HZ at smaller separations, thereby altering the secular forcing frequency from the binary companion. In addition, the planetary spin precession frequency for the 24-h rotator increases from ∼10 to ∼46 arcsec yr^{-1} (see Quarles et al. (2019) for more details). We expand our investigation with an Earth-analogue orbiting α Cen B to include three planetary inclinations (2°, 10°, and 30°) so that we sample a broader range of potentially habitable orbital configurations.

4.1 Factors affecting Milankovitch cycles

The evolution of the planetary eccentricity and obliquity can correlate with changes in the global mean surface temperature through seasonal changes to the incoming radiation. In addition, the global mean ice fraction $f_{\rm ice}$ and global mean albedo affect the global surface temperature by modifying the contribution of the outgoing radiation. Fig. 6 demonstrates these variations for a modern, moonless Earth-analogue ($\varepsilon_o = 23°$, $\gamma = 46\,{\rm arcsec\,yr^{-1}}$) with an inclination i_p of 2° (black), 10° (red), and 30° (blue). For 30° (blue; Fig. 6a), the eccentricity variation is larger, but the magnitude of the planetary eccentricity remains small. The obliquity variation increases as a function of i_p in Fig. 6(b), where we expect the maximum variation to scale with twice the planetary inclination ($\Delta\varepsilon \sim 2i_p$). Similar to Fig. 1, the planet's eccentricity and obliquity variation induces oscillations in the global surface temperature (Fig. 6c), where the temperature changes are mild for low mutual inclination ($\lesssim 10°$; red and black).

A planetary orbit with a larger mutual inclination (30°; blue) undergoes apsidal and nodal precession, which allows for stark changes in surface temperature and a larger variation. Planets orbiting α Cen B reach a steady state with respect to the global ice fraction $f_{\rm ice}$ and albedo α after the first 100 kyr. Interestingly, Fig. 6(d) shows that the low mutual inclination ($\lesssim 10°$; red and black) cases have a higher mean $f_{\rm ice}$ than the larger mutual inclination (30°; blue). This subsequently manifests in a higher average global albedo (Fig. 6e). The larger mutual inclination (30°; blue) planet has a maximum $f_{\rm ice} \sim 0.12$, but the global albedo can fluctuate over a 1000-yr interval between ∼0.32 and 0.36. In fact, the larger mutual inclination (30°; blue) planet experiences transient ice-free states (Fig. 6d) that correlate with the mean value of the assumed albedo parameters for land and water (i.e. $[\alpha_L + \alpha_W]/2$; Table 1). The mean global albedo in the larger mutual inclination (30°; blue) simulation is lower (Fig. 6e) in response to the smaller global ice fraction (Fig. 6d).

Figs 7–9 demonstrate the time evolution of the planetary eccentricity and obliquity, which affect the evolution of the COPP (Figs 7c, 8c, and 9c), surface temperature with latitude (Figs 7d, 8d, and 9d), and the ice mass with latitude (Figs 7e, 8e, and 9e) for each respective planetary inclinations (2°, 10°, and 30°). Each of the cases presented (Figs 7–9) have identical spin precession constants (46 arcsec yr^{-1}), but have different orbital precession frequencies. In Fig. 7(c), the COPP is largely correlated with the ∼6° obliquity variation (Fig. 7b), which is imprinted in the variations of surface temperature (Fig. 7d) near the equator and the poles. Fluctuations in the ice mass (Fig. 7e) exhibit Milankovitch cycles similar to Earth's, where the variation in the polar cap is due to a combination of precessions from the orbit and obliquity.

A planet inclined by 10° experiences larger obliquity variations (∼18°; Fig. 8b), but the COPP frequency increases due to the faster orbital precession (Fig. 8c). Consequently, the planet has stronger fluctuations in the surface temperature (Fig. 8d) and ice mass (Fig. 8e). The persistence of the polar caps is unaffected, but the extent and duration of interglacial periods at 50° latitude are increased due to the larger obliquity variation and faster orbital precession. A planet inclined by 30° has obliquity variations of 50° from nodal precession, but the apsidal locking at the forced eccentricity is much weaker and allows for more substantial eccentricity variations (Figs 9a and b). The COPP is no longer only affected by the differing precession rates resulting in a more complex evolution (Fig. 9c). The more dramatic obliquity variation results in periodic cooling and warming of the high latitudes corresponding to low and high points in the obliquity evolution (Fig. 9d). Thus, there are polar caps for brief periods followed by much longer interglacial periods. Since the obliquity rises above 55° (Williams & Pollard 2003; Rose et al. 2017; Kilic et al. 2018), ice coverage accumulates around the equator to form a so-called 'ice belt' (Fig. 9e). Similar to the polar caps, the ice belt is short lived and there is a brief ice-free period between the two states. The time-scale to cycle through all three ice distribution states (∼25 000 yr) and happens to be ∼1.5 times the induced orbital precession from the binary companion (∼17 000 yr).

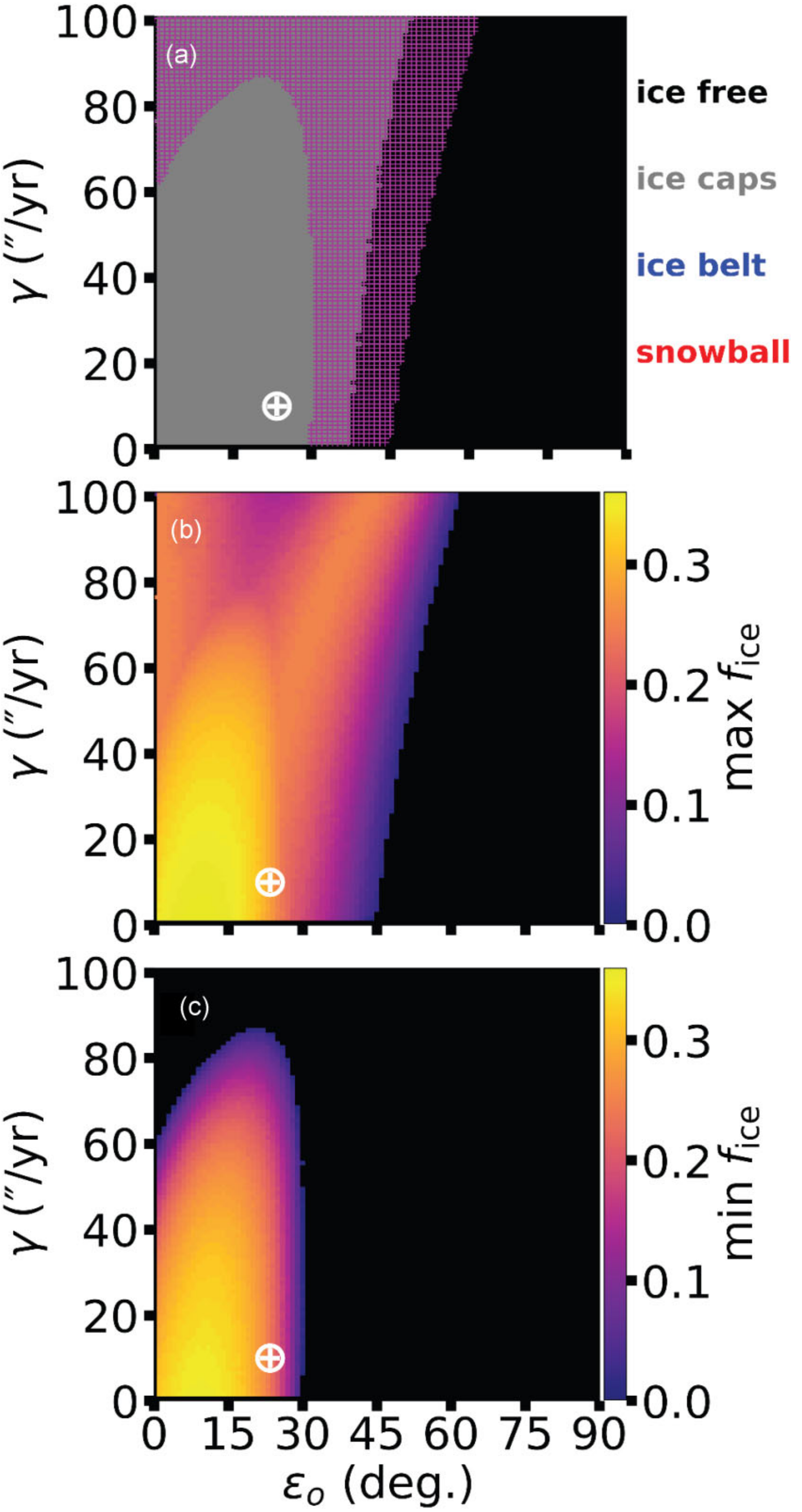

Figure 5. Categorization of the most frequent ice distribution state (ice-free, ice caps, ice belt, or snowball) within each simulation in panel (a). Panels (b) and (c) illustrate the maximum and minimum global ice fraction, respectively. The magenta hatched region plotted in panel (a) represents the cases where the planet oscillates between two ice distribution states. Labels for ice belt and snowball are provided for consistency with Fig. 12, although none of the simulations represented here enter either of these states.

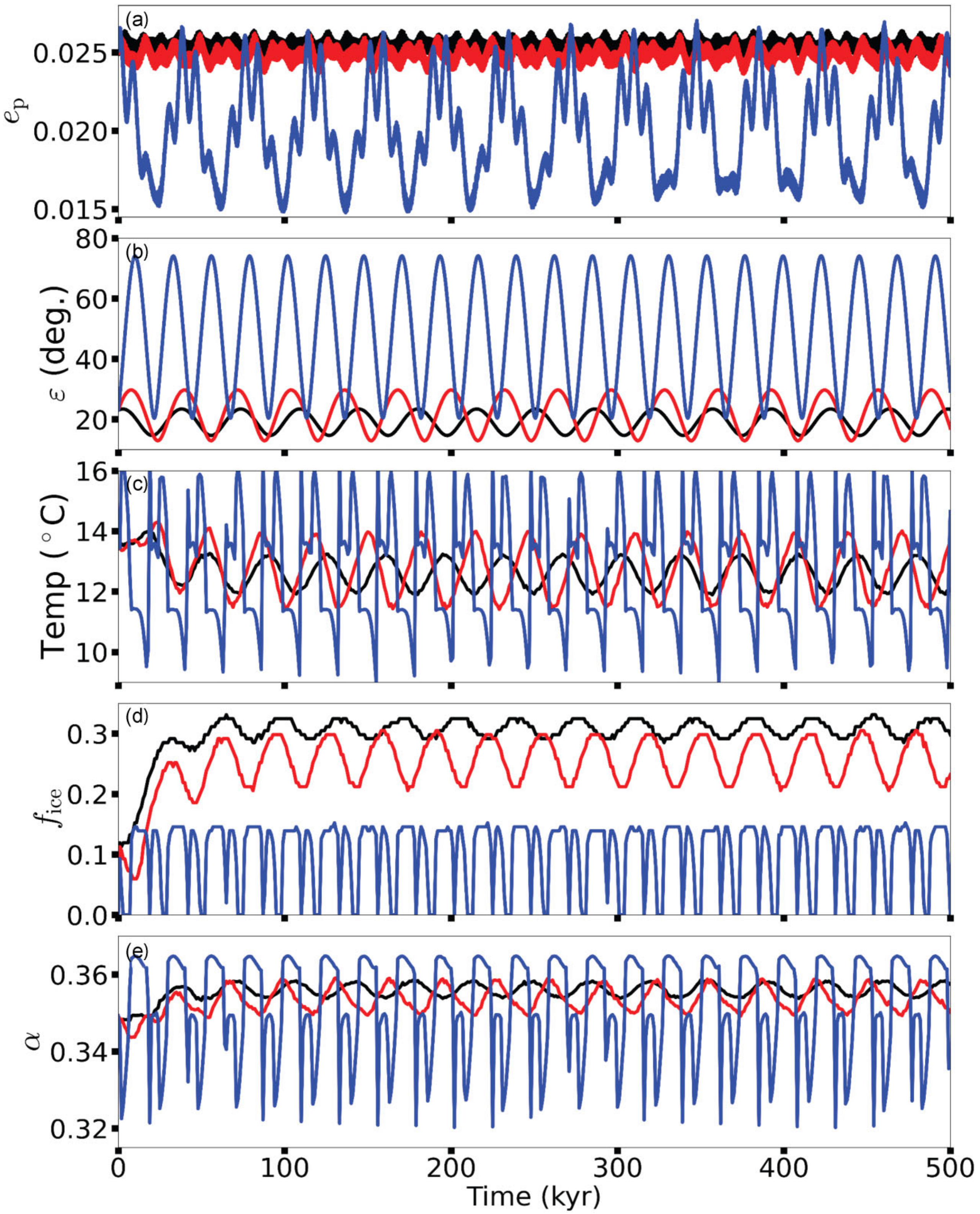

Figure 6. Evolution over a 500 kyr time-scale of the (panel a) planetary eccentricity e_p, (panel b) obliquity ε, (panel c) global surface temperature, (panel d) global ice fraction f_{ice}, and (panel e) global albedo α. The planetary orbit begins near its forced eccentricity at the inner edge of α Cen B's HZ with an inclination of 2° (black), 10° (red), and 30° (blue). The initial planetary obliquity ε and precession constant γ are similar in value to a modern, moonless Earth (23° and 46 arcsec yr^{-1}, respectively).

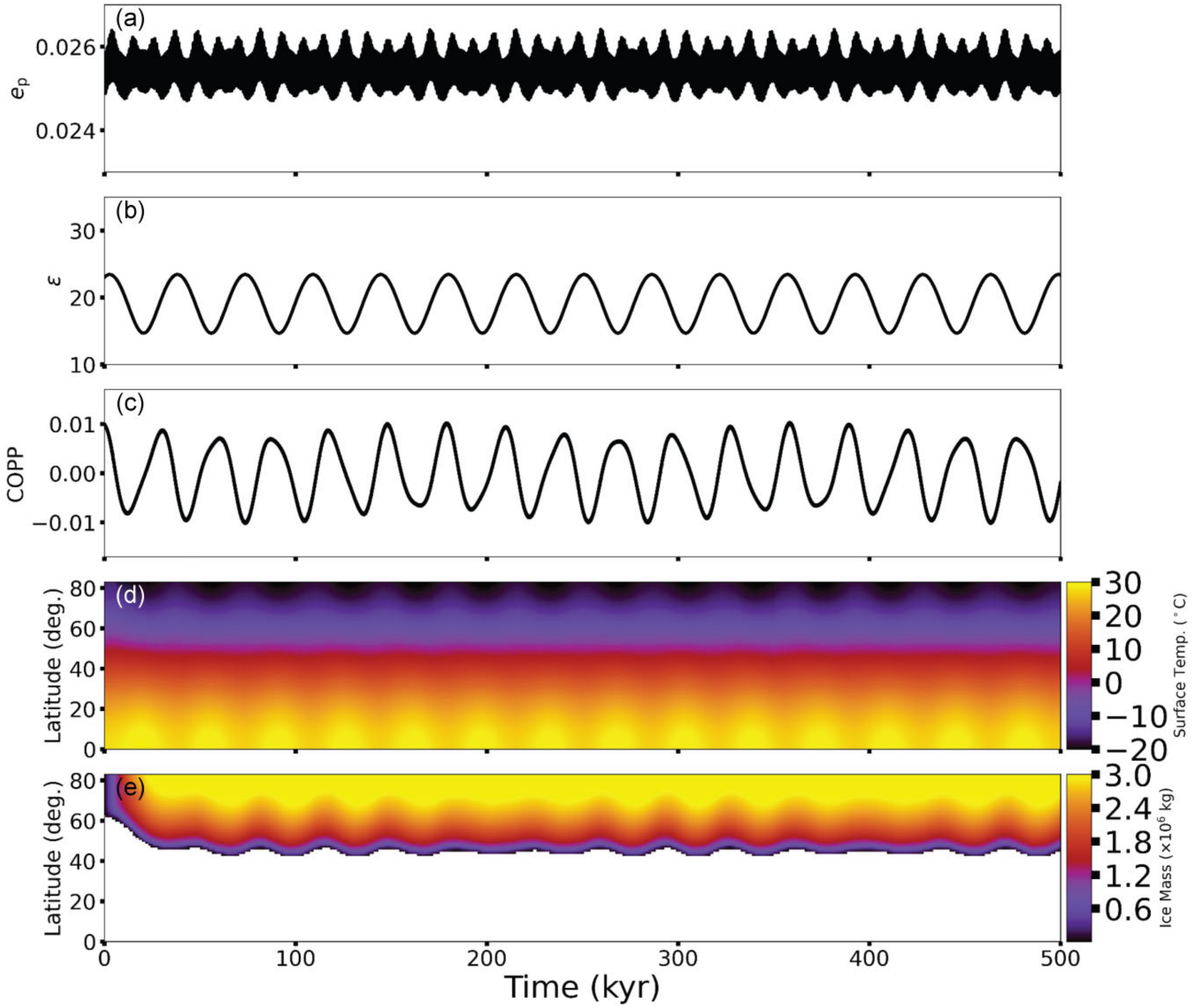

Figure 7. Simulation of an Earth-analogue ($\varepsilon = 23^\circ$) initially inclined 2° above the binary orbital plane showing the evolution in the (panel a) planetary eccentricity e_p, (panel b) obliquity ε, (panel c) COPP ($e_\mathrm{p}\sin(\varepsilon)\sin(\varpi_\mathrm{p} + \psi)$), (panel d) latitudinal surface temperature, and (panel e) latitudinal ice mass. The white cells in panel (d) represent latitudes with very little ice accumulation ($<10^4$ kg) or 'ice-free'.

4.2 Obliquity and global surface temperature variation

For an Earth-analogue in α Cen A's HZ, the obliquity variations are relatively moderate ($\lesssim 40^\circ$), even when considering a wide range of precession constants. The HZ for α Cen B is more interesting because it allows for overlap in the secular orbital and spin precession frequencies so that larger obliquity variations are possible (Quarles et al. 2019). We perform simulations for a broad range of precession constants and initial prograde obliquities following the same procedure discussed in Section 3.2, but for three planetary inclinations (2°, 10°, and 30°). Fig. 10 shows the obliquity variation ($\Delta\varepsilon$) and global surface temperature variation (ΔT) using our numerical simulations over 500-kyr time-scales, where the column labels denote the initial planetary inclination relative to the binary orbital plane. The white $\oplus$ symbol designates initial parameters corresponding to a modern, moonless Earth-analogue in terms of the precession constant (46 arcsec yr^{-1}) and initial obliquity (23°). Fig. 10(a) clearly shows the strip of low obliquity variation expected from strong spin-orbit coupling, which intrudes upon a broader region of increased obliquity variation at high spin precession constants (yellow-light blue) and these higher variations are due to a spin-orbit resonance with the binary. Fig. 10(b) reproduces some of our previous results (see Quarles et al. 2019 for more details), while Fig. 10(c) illustrates that moderate to large obliquity variations ($\Delta\varepsilon > 15^\circ$) are ubiquitous for high-inclination planets due to the nodal orbital precession. Moreover, some combinations of spin precession and initial obliquity (magenta regions in Fig. 10c) allow for the full range of prograde obliquity to be explored.

The obliquity variation in Figs 10(a)–(c) presents one aspect, where our calculations using a climate model introduces another facet when considering the potential climate for an Earth-analogue orbiting α Cen B. The global surface temperature variation (ΔT) in Fig. 10(d) is limited to ~6°, where these variations largely occur when the obliquity variation is high. However, larger ΔT values also occur within the strip for strong spin-orbit coupling; these variations extend to low spin precession constants for initial obliquity of ~30°–35°. Our investigation of the ice distributions for an Earth-analogue orbiting α Cen A (see Section 3.3) uncovered oscillations between states, which are the likely cause for the additional structure seen here.

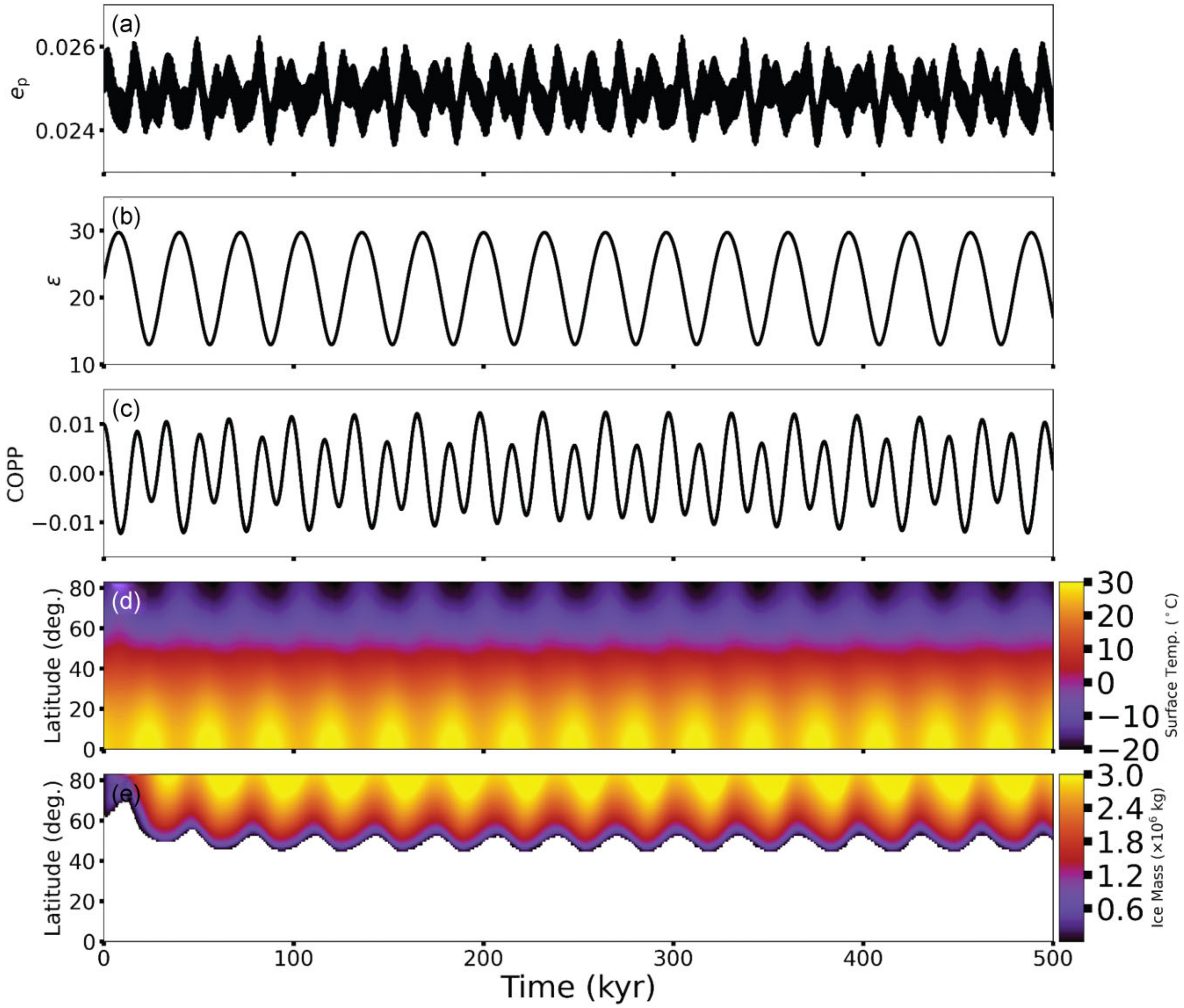

Figure 8. Similar to Fig. 7, but for an Earth-analogue initially inclined 10° above the binary orbital plane.

Figs 10(e) and (f) show that increased obliquity variation can lead to more extreme changes in the global surface temperature, where the tan regions signify simulations that begin with Earth-like global surface temperatures, but undergo climate feedbacks that force the planet into a snowball state (tan regions). In particular, the regions for an Earth-analogue to enter a snowball are especially large in Fig. 10(f), where a modern, moonless Earth-analogue lies near a transition region of large temperature variation (∼5°; Fig. 9) and a snowball state. Thus far, our discussion is limited to a moonless Earth-analogue and adding a Luna-like moon (i.e. similar in mass and orbital separation to our Moon) would transport some the planet across various transition regions. Quarles et al. (2019) showed the precession constant for an Earth-analogue orbiting α Cen B with a Luna-like moon is ∼84 arcsec yr^{-1}, so such a moon would drastically reduce the potential for habitability of an Earth-analogue around α Cen B, in contrast to current conditions for the Earth–Moon system.

The tan strips for low precession constant ($\gamma \lesssim 1$ arcsec yr^{-1}) could be spurious due to assumptions within `POISE` concerning the planetary rotation period becoming commensurable with the orbital period. For an Earth-analogue orbiting at the inner edge of α Cen B's HZ, a 2 arcsec yr^{-1} spin precession constant corresponds to an ∼24-d rotation period, which is an order of magnitude smaller than the orbital period and is consistent with the physical assumptions made by the developers of `POISE`.

4.3 Ice fraction and distributions

Moderate changes in the global surface temperature over time can correlate with variations in the global ice fraction (see Fig. 6). Fig. 11 broadly mimics the structures shown in the Figs 10(d)–(f) for the respective planetary mutual inclination. However, Figs 11(a) and (b) show more detail surrounding the main structures. There are also particular regions where the global ice fraction $f_{\rm ice}$ changes very little ($\Delta f_{\rm ice} \lesssim 0.01$), in contrast to the yellow regions ($\Delta f_{\rm ice} = 1$ and $\Delta\alpha = 0.3$) that mark configurations that transition to snowball states. The global albedo directly affects the calculation of the global surface temperature, and thus it is unsurprising that Figs 11(d)–(f) are highly correlated with 10(d)–(f).

Examining the variation in the global ice fraction uncovers the major structure across the full range of initial parameters (ε_o, γ) for the planetary spin states, but it leaves many questions. Fig. 12 shows the ice distribution categories, maximum global ice fraction,

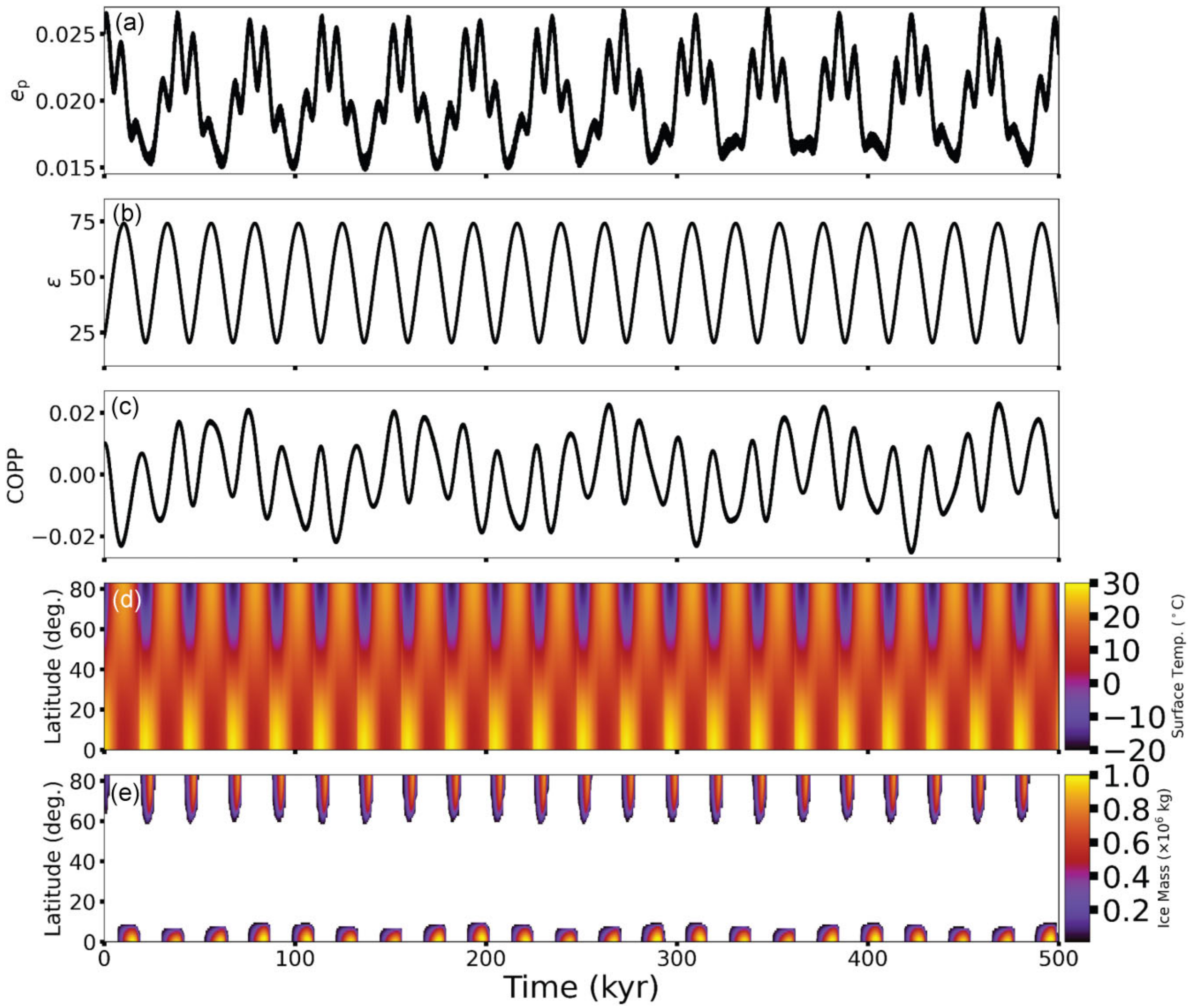

Figure 9. Similar to Fig. 7, but for an Earth-analogue initially inclined 30° above the binary orbital plane.

and minimum global ice fraction in a similar manner as Fig. 5, but for an Earth-analogue orbiting α Cen B and for our three planetary mutual inclinations by column. There is also a white ⊕ symbol to mark initial conditions for a modern, moonless Earth-analogue. For nearly coplanar systems (Figs 12a–c), we find a broad zone with ice caps for $\varepsilon_o \lesssim 30^\circ$, with ice-free states for $30^\circ \lesssim \varepsilon_o \lesssim 60^\circ$, and with an ice belt for $60^\circ \lesssim \varepsilon_o \lesssim 90^\circ$. Some slow rotators ($\gamma \lesssim 5\,\mathrm{arcsec\,yr^{-1}}$) can enter snowball states, but these conditions likely need more sophisticated models or at least an independent means of verification. The panels illustrating the maximum and minimum $f_{\rm ice}$ are colour-coded, where black and red corresponds to an exactly ice-free or snowball state, respectively. The bridge in Fig. 12(b) for high γ and moderate ε_o forms due to the obliquity variation (see Fig. 10a). The common regions between Fig. 12(b) and (c) show which conditions can form stable ice caps (low ε_o) or an ice belt (high ε_o). The difference regions between Fig. 12(b) and (c) show the limits of variation, where an Earth-analogue oscillates between two or three states (magenta hatching). Moreover, the regime that oscillates between ice-free and ice caps highlights the respective structure observed in Figs 10(d), 11(a), and (d). Note that the background colour signifies the most frequent state within our simulation, where the oscillation between ice distribution categories can go both ways.

Increasing the planet mutual inclination to 10° allows for larger obliquity variation, which enables a greater diversity of ice distribution states. Figs 12(d)–(f) shows that the regime for primarily ice caps increases and an ice belt decreases. The snowball regions correspond to most conditions that produce the most extreme obliquity variations (see Fig. 10b). Due to the overall higher obliquity variation, more of the parameter space can be ice-free at times (Fig. 12f), which suggests a greater potential for interglacial events. The presence of a Luna-like moon could change an Earth-analogue from a planet with perpetual ice caps to one with transient ice caps and ice-free states being more frequent. Our simulations show that snowball states become drastically more likely (due to higher obliquity variations; Fig. 10c) for a highly inclined ($i_p = 30^\circ$) Earth-analogue, where a 24-h rotator lies within a transition region (see Fig. 9e). Perpetual ice caps are absent, while there is a much smaller regime for perpetually ice-free states (black region near $\varepsilon_o \sim 45^\circ$ in Fig. 12g). Fig. 12(h) shows that less of the planet's surface can support ice, unless the Earth-analogue is in either a snowball state or a fast rotator ($\gamma \gtrsim 80\,\mathrm{arcsec\,yr^{-1}}$).

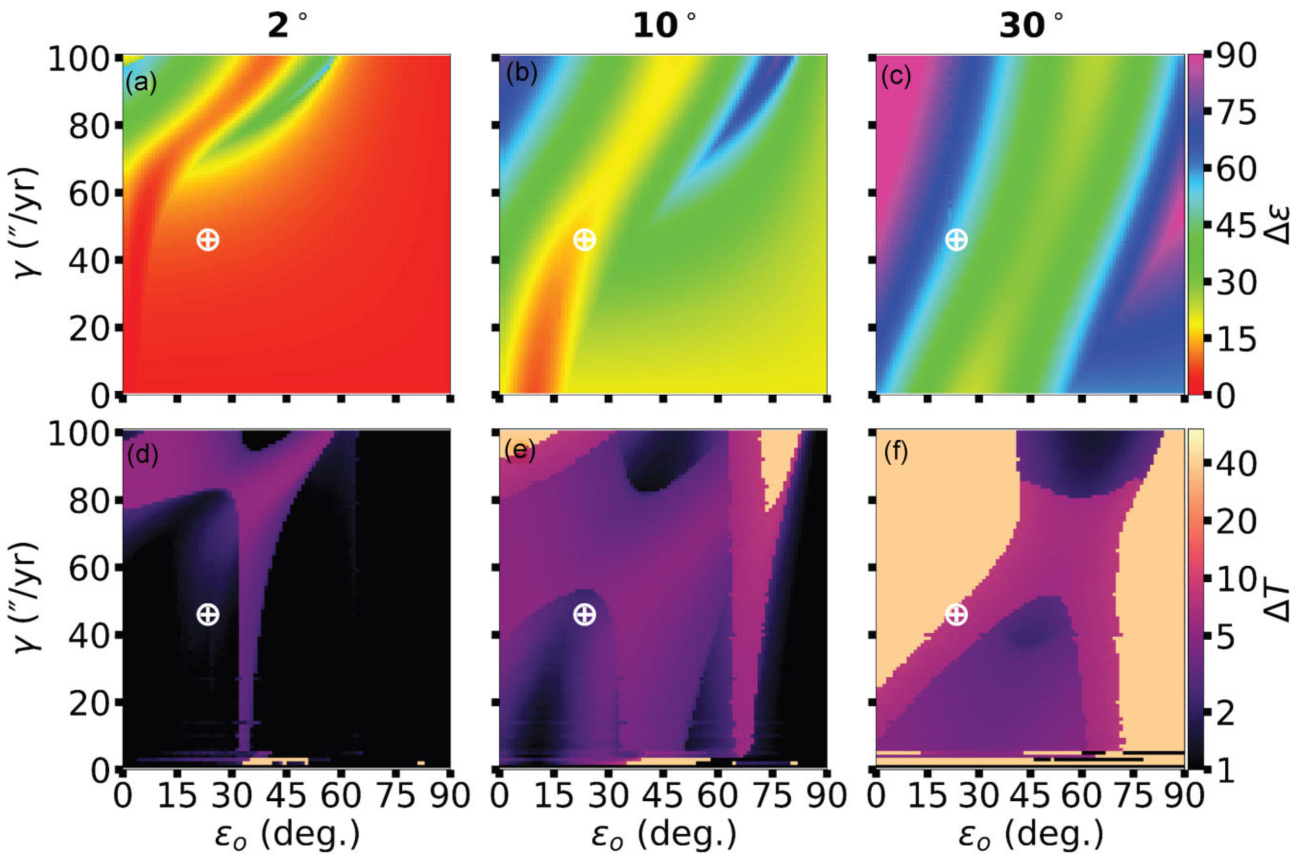

Figure 10. Obliquity and global surface temperature variation for an Earth-analogue orbiting α Cen B over 400 kyr, where the planet's orbit is inclined by 2°, 10°, or 30° relative to the binary orbit. The obliquity variation $\Delta\varepsilon$ (panels a–c) changes with the orbital inclination, with a valley of minimum variation resulting from orbital precession (Quarles et al. 2019). The global surface temperature variation ΔT (panels d–f) largely correlates with the obliquity variation for a respective inclination. The white $\oplus$ symbol designates conditions ($\varepsilon_o = 23°$, $\gamma = 46\,\mathrm{arcsec\,yr^{-1}}$, $P_{\rm rot} \sim 24$ h) for a modern, moonless Earth. Note that the colour scales are different in this figure and Fig. 11, when comparing with a similar figure for Star A (Fig. 4).

5 AN EARTH-ANALOGUE ORBITING THE SECONDARY STAR OF α CENTAURI-LIKE BINARIES

The general population of Sun-like stellar binaries spans a large range in mass ratio, orbital period (or semimajor axis), and eccentricity (Raghavan et al. 2010; Moe & Di Stefano 2017). Quarles et al. (2019) explored the obliquity variations for an Earth-analogue orbiting the more massive and luminous stellar component, star A. In this work, we investigate the obliquity variations for an Earth-analogue orbiting the secondary component, star B, and identify the possible consequences for the ice distributions including the Milankovitch cycles. A range of binary semimajor axis and eccentricity values are used (see Section 2.1), but we use stellar masses and luminosities that are identical to those for α Centauri AB. The initial spin state begins with a 23° obliquity and 46 $\mathrm{arcsec\,yr^{-1}}$ spin precession constant, which is consistent with a modern, moonless Earth-analogue.

5.1 Factors affecting milankovitch cycles

Milankovitch cycles for the Earth are shaped mainly by the evolution in its eccentricity and obliquity (Milankovitch 1941), where the variations in these components are correlated with perturbations from neighboring terrestrial planets and Jupiter (Laskar et al. 1993; Deitrick et al. 2018a). Deitrick et al. (2018b) showed that a large planetary eccentricity (>0.1) can trigger snowball states or even asymmetries in coverage of the ice caps. For the case considered herein, there are no other planets but the stellar companion drives the orbital and spin evolution (Andrade-Ines et al. 2016; Quarles et al. 2019). Extreme obliquity variations can arise for the Earth-analogue due to a spin-orbit resonance with stellar binary. Figs 13–15 show the time evolution of the (panel a) planetary eccentricity, (panel b) obliquity, (panel c) COPP, (panel d) surface temperature, and (panel e) ice mass in a similar manner as in Sections 3 and 4, but the binary semimajor axis is varied from 20, 25, and 30 AU, while the binary eccentricity begins at 0.2. The Earth-analogue begins on a circular orbit that is inclined 10° relative to the binary orbital plane. The eccentricity variations for the Earth-analogue remain quite low ($\leq$0.02) and decrease substantially as the binary orbital semimajor axis increases, so the forced eccentricity plays a minor role in the climate evolution.

Fig. 13 shows the planetary eccentricity changes with the secular forcing time-scale (~15 000 yr) from the binary companion in Fig. 13(a), while obliquity variation time-scale is a bit longer in Fig. 13(b). These factors combine, along with their associated precession rates, to produce a more complex COPP in Fig. 13(c) that drives variations in the surface temperature (Fig. 13d) and ice mass (Fig. 13). In this simulation, the Earth-analogue develops polar caps that are persistent and the ice latitude (i.e. border between white and colored cells) in Fig. 13(e) correlates with the ~18° obliquity variation (Fig. 13b).

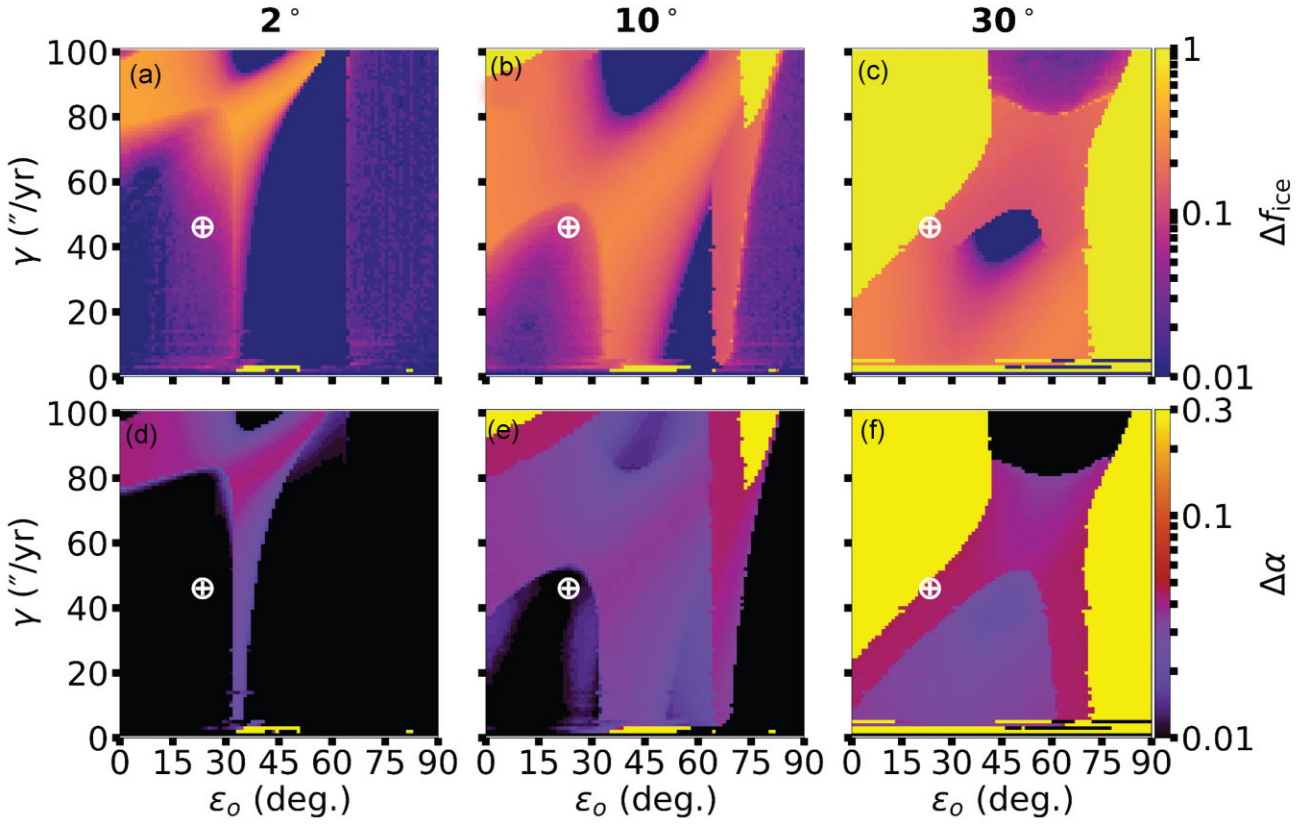

Figure 11. Similar to Fig. 10, but for the global ice fraction $\Delta f_{\rm ice}$ (panels a–c) and albedo $\Delta\alpha$ (panels d–f) variations. The white ⊕ symbol designates conditions ($\varepsilon_{\rm o} = 23^\circ$, $\gamma = 46$ arcsec yr^{-1}, $P_{\rm rot} \sim 24$ h) for a modern, moonless Earth.

Increasing the binary semimajor axis to 25 AU (Fig. 14) reduces the magnitude and frequency of the eccentricity variations (Fig. 14a). Consequently, the secular precession frequency begins to approach the spin precession frequency, which causes an increase in the obliquity variation ($\Delta\varepsilon \sim 30^\circ$; Fig. 14b). The climate precession frequency decreases (Fig. 14c), although a similar structure exists that is due to the linear combination of frequencies. A longer climate precession time-scale and larger obliquity variation permits the Earth-analogue to oscillate between a warm and temperate climate (Fig. 14d). The warmer climate occurs when the obliquity reaches 40°–60° and the polar caps completely disappear. In this state, the equatorial latitudes are cooler, but the poles are significantly warmer. Once the obliquity decreases below 40°, the temperature at high latitudes drops low enough to allow for polar caps to regrow. Fig. 14(e) shows the cycle between interglacial (ice-free) states and transient polar caps.

The secular forcing frequency due to the binary companion overlaps with the spin precession frequency at ∼30 AU, which induces the largest obliquity variations. The forced eccentricity oscillations (Fig. 15a) with a 30-AU binary separation are small and the ∼60° obliquity variation (Fig. 15b) largely determines how climate evolves on the Earth-analogue. The COPP undergoes cycles every ∼125 kyr (Fig. 15c), but the diminished magnitude of the maximum eccentricity reduces its influence upon the Milankovitch cycles. Fig. 15(b) shows the planetary obliquity rises above 55° for a significant portion of its cycle, which leads to the formation of an ice belt instead of an ice cap (Kilic et al. 2018). Fig. 15(d) illustrates this transition, where the equatorial latitudes have a much higher surface temperature for low obliquity and drop to freezing temperatures once the obliquity increases enough. As a result, the Earth-analogue develops small ice caps that eventually disappear, which is followed by a significant ice belt (Fig. 15e). As the obliquity decreases, we might expect the ice belt to fully ablate followed by the growth of an ice cap (see Fig. 9e). However, this is not the case because the ablation rate of the ice belt is too slow (i.e. thermal inertia of the ice belt is high). Under these conditions, the ice cap begins to grow before the ice belt disappears and an ice-albedo feedback prevents the return to an ice cap dominated state (i.e. a majority of the surface is ice covered, which stops the heat flow across latitudes). Instead, the Earth-analogue enters a snowball state, which persists indefinitely in our simple model. Deitrick et al. (2018b) showed a similar ice instability for dynamically hot planetary systems orbiting a single G dwarf. We illustrate one pathway to a snowball state, but this is not destiny for all planets because of the limitations of our climate model that are calibrated for Earth-like conditions and other features (e.g. land/ocean fraction, CO_2 warming, land distribution) could change the heat flow across latitudes.

5.2 Obliquity and global surface temperature variation

For an Earth-analogue within a binary star system, significant obliquity variations exist when the secular forcing frequency from the binary is larger than the spin precession frequency (i.e. $g_s \gtrsim \gamma$). Quarles et al. (2019) showed this feature for an Earth-analogue orbiting the more massive star; herein we perform a similar investigation of an Earth-analogue orbiting the less massive star in Fig. 16(a). The white cells in each panel of Fig. 16 are not evaluated due to orbital instabilities within the host star's HZ (Quarles et al. 2020b). Closely separated binaries ($a_{\rm bin} = 10$–20 AU) induce moderate obliquity variations ($\Delta\varepsilon \sim 20^\circ$–40°), while there is a yellow

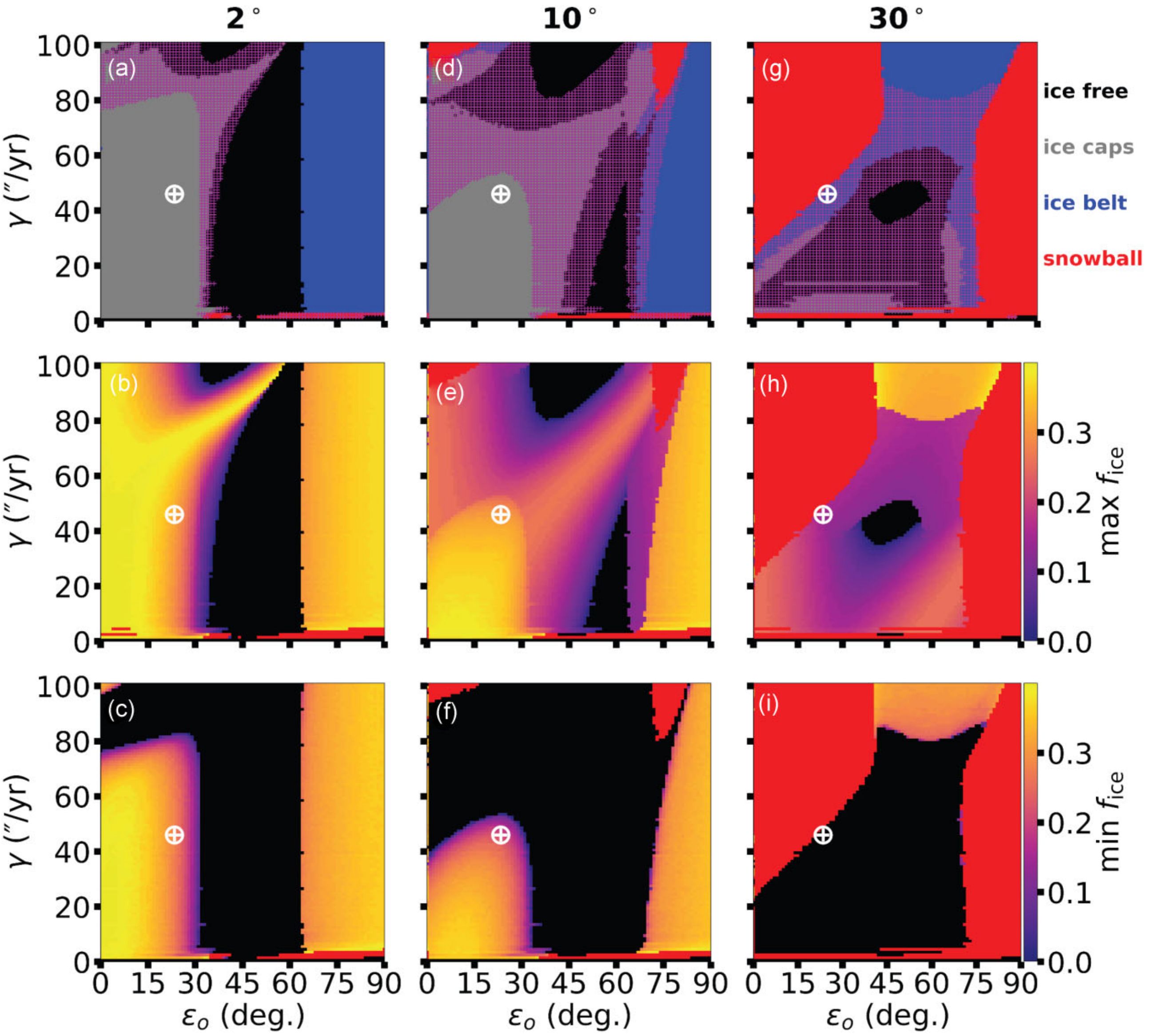

Figure 12. Similar to Fig. 5, but examining differences in the most frequent ice distribution state (ice-free, ice caps, ice belt, or snowball) as well as the maximum and minimum global ice fraction for a Earth-analogue orbiting α Cen B inclined by 2°, 10°, and 30° relative to the binary orbital plane. The magenta hatched region plotted in panel (a) represents the cases where the planet oscillates between two or three ice distribution states.

strip of lower obliquity variation ($\Delta\varepsilon \sim 15°$) beginning at 20 AU. This strip occurs when the planetary spin axis precession more closely follows the orbital precession (i.e. stronger spin-orbit coupling). The curvature of the strip stems from how the secular forcing frequency g_s depends on the binary semimajor axis, $a_{\rm bin}$, and eccentricity, $e_{\rm bin}$. For $a_{\rm bin} = 22$–27 AU, the obliquity variation increases to ∼45°, and the highest variation occurs for $a_{\rm bin} = 28$–31 AU due to a spin-orbit resonance. For most configurations with $a_{\rm bin} > 40$ AU, the spin-orbit coupling is stronger, which limits the obliquity variation to a few degrees.

The global temperature (Fig. 16b) and ice fraction variation (Fig. 16c) largely correlate with the obliquity variations in Fig. 16(a). The global temperature can oscillate by 5°C–10°C (purple), decrease dramatically by 40° (tan), or remain nearly constant (black) in response to the changes in obliquity. The large obliquity variations due to the spin orbit resonance force the large global temperature change through ice-albedo feedbacks (see Section 5.1 and Fig. 15). We find the global temperature variations broadly correlate with changes in the global ice fraction (Fig. 16c).

5.3 Ice fraction and distributions

Following Sections 3.3 and 4.3, we examine the ice distribution within four categories (ice-free, ice caps, ice belt, and snowball), but through the parameter space of varying the binary orbit. Fig. 16(d) shows the most common state for a modern, moonless Earth-analogue is having perpetual ice caps (grey) with a varying degree of Milankovitch cycles (i.e. periodic growth/retreat at the ice latitudes), while the least common is having an ice belt. This outcome could be flipped if a sufficiently high initial obliquity was used. An Earth-analogue enters a snowball (red) state when the obliquity variation is $\gtrsim 50°$, which occurs when the obliquity is $>55°$ for a significant portion of the obliquity variation cycle. Ice-free states (black) are possible for moderate obliquity variation, when the obliquity is

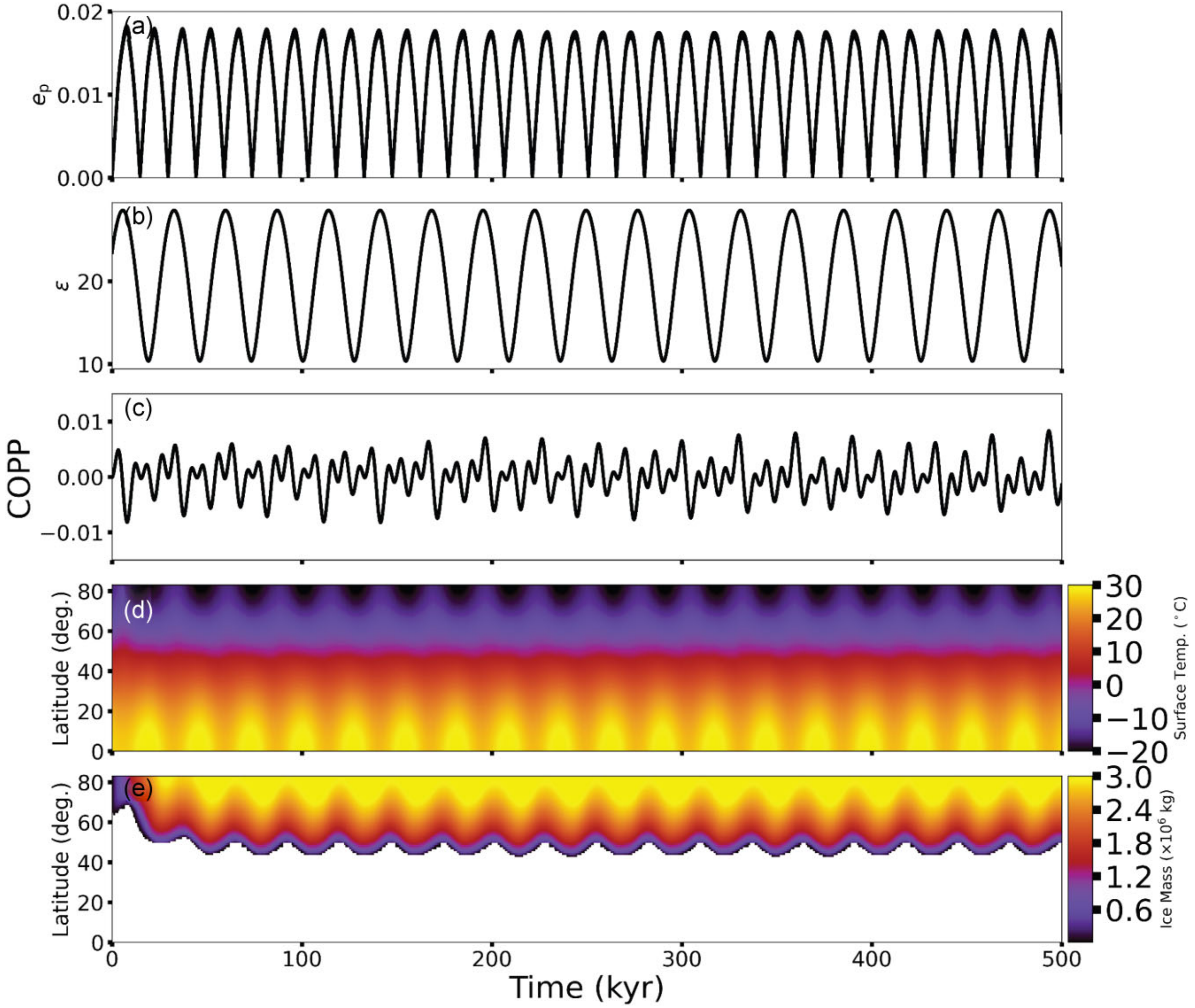

Figure 13. Evolution over 500 kyr of the (panel a) planetary eccentricity, (panel b) obliquity, (panel c) COPP ($e_{\rm p}\sin(\varepsilon)\sin(\varpi_{\rm p}+\psi)$), (panel d) surface temperature, and (panel e) ice mass for an Earth-analogue orbiting the secondary star in an α Centauri-like system. The planet begins on an inclined, circular orbit that is tilted 10° relative to the binary orbital plane with a binary semimajor axis and eccentricity equal to 20 AU and 0.2, respectively. The initial planetary spin state is analogous to a modern, moonless Earth ($\varepsilon_{\rm o} = 23^\circ$, $\gamma = 46$ arcsec yr^{-1}).

between 40°–55° for a significant portion of the obliquity variation cycle. Surrounding the region for spin-orbit resonance, an Earth-analogue can transition between states for ice-free, ice caps, and an ice belt as designated by the magenta symbols.

Figs 16(e) and (f) show the extremes in the global ice fraction $f_{\rm ice}$. When the orbital perturbations on the Earth-analogue are greatest ($a_{\rm bin} < 20$ AU), the global ice fraction oscillates between 0.15 and 0.38. For lower obliquity variations ($\Delta\varepsilon \sim 15^\circ$), the global ice fraction varies slightly (see Fig. 13e), and ice caps cover about 1/3 of the total surface. Comparing the 20–40 AU region of Figs 16(d)–(f), the extent of the most common ice distributions can be deduced, where the largest extent of ice covers 1/5 of the total surface and ice-free states are possible. When $a_{\rm bin} > 40$ AU, ice caps dominate with little variation in their extent ($f_{\rm ice} = 0.1$–0.2). Currently, the global ice fraction on Earth is ∼0.1, but this fraction was larger in the recent geologic past (10 kyr ago) during an ice age with a northern ice cap that extended from 90°N to 45°N to create the Great Lakes.

6 CONCLUSIONS

The potential habitability of an Earth-analogue is defined by the planet's ability to host liquid water upon its surface, and orbital perturbations can potentially alter a planet's habitability through Milankovitch cycles (i.e. growth/retreat of ice). We investigate the obliquity evolution of a circumstellar Earth-analogue within α Centauri-like binaries near the inner edge of the respective host star's HZ, where a variable obliquity can induce changes in the global ice fraction and thereby modify the global surface temperature. Our simulations explore a wide range of spin states varying the initial obliquity, $\varepsilon_{\rm o}$, and spin precession constant, γ. We identify initial spin states for an Earth-analogue that allow it to sustain persistent ice at either high latitudes (ice caps) or near the equator (ice belt; ?; Rose et al. 2017; Kilic et al. 2018) using a one-dimensional EBM called `POISE` within `VPLanet` (Deitrick et al. 2018b; Barnes et al. 2020). Some initial spin states remain ice-free or evolve into snowball states, where the latter could dramatically limit a planet's habitability. Note

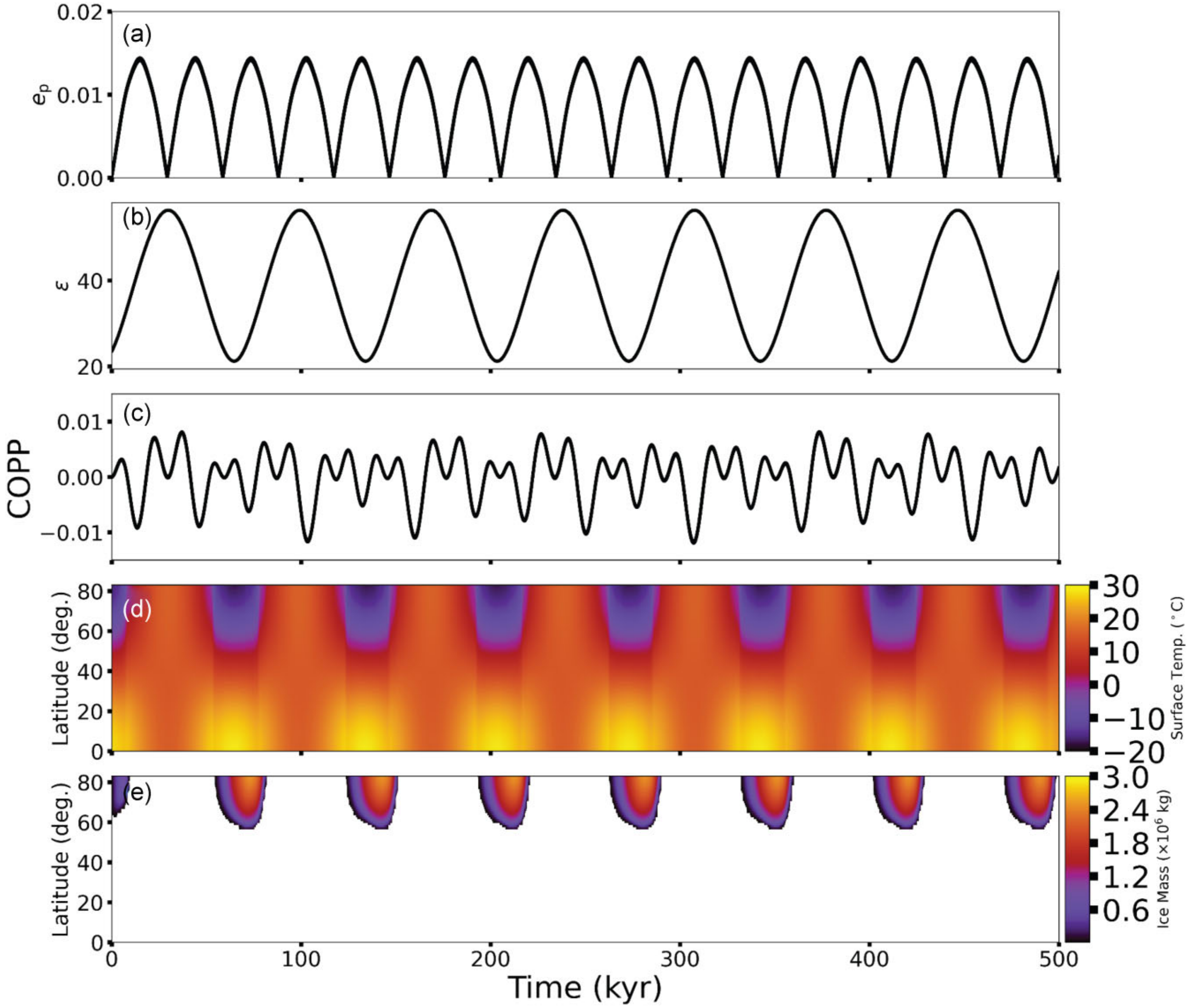

Figure 14. Similar to Fig. 13, but the binary semimajor axis is 25 AU.

that our usage of *ice cap* is different than the Earth science community and refers to ice coverage beginning at a pole and extending towards the equator.

The obliquity variation ($\Delta\varepsilon$) is fairly mild for an Earth-analogue inclined by 10° orbiting within the HZ of α Cen A (see Fig. 4) and is largely driven by the nodal precession induced by the stellar companion ($\Delta\varepsilon \sim 2i_{\rm p}$). The maximum obliquity variation is ∼30° over 20-kyr time-scale, which limits changes in the globally averaged ice fraction ($\Delta f_{\rm ice} \lesssim 0.2$) and surface temperature ($\Delta T < 6$°C). Since the changes in ice fraction are small (mostly at border regions of ice caps), the resulting changes in albedo are also small (< 3 per cent). An Earth-analogue can have persistent ice caps for low initial obliquity ($\lesssim 30°$) or can be completely ice-free for high initial obliquity (>60°). Between these extremes, the global ice distribution can oscillate from ice-free to ice caps (or vice versa) depending on the planet's initial obliquity and rotation rate (through the spin precession constant γ). The Milankovitch cycles can be extreme for high γ with growth/retreat of polar caps by ∼20° of latitude.

For an Earth-analogue orbiting α Cen B, we find a more dynamic range of obliquity variation that depends on the initial inclination (see Fig. 10). The obliquity evolution is driven by nodal precession in broad regions, but these are interrupted by valleys of low variation due to strong spin-orbit coupling (Quarles et al. 2019) and peaks of high obliquity variation from a spin-orbit resonance with the host binary. We investigate three orbital inclinations (2°, 10°, and 30°). A nearly coplanar (2°) Earth-analogue orbiting α Cen B evolves in a similar manner to one orbiting α Cen A, but high initial obliquity (>65°) states produce an ice belt instead of ice caps (Fig. 12). An Earth-analogue inclined by 10° can be in a snowball or ice-free state within two pockets within the parameter space. Many initial spin states allow for the Earth-analogue to transition periodically between ice-free, ice caps, and an ice belt. A highly inclined (30°) Earth-analogue can enter a snowball state for a much broader set of initial parameters. Due to the higher overall obliquity variation ($\Delta\varepsilon \sim 60°$), the region dominated by an ice belt moves to lower initial obliquity. Initial spin states that permit persistent ice caps become quite rare with a higher orbital inclination, and periodic transitions between ice distribution states becomes common (except when a snowball is formed). The Milankovitch cycles for a low inclination, moonless Earth-analogue (24-h rotator) are not drastic, but the cycles for an Earth-analogue with a faster rotation or a higher initial obliquity allow transitions between states.

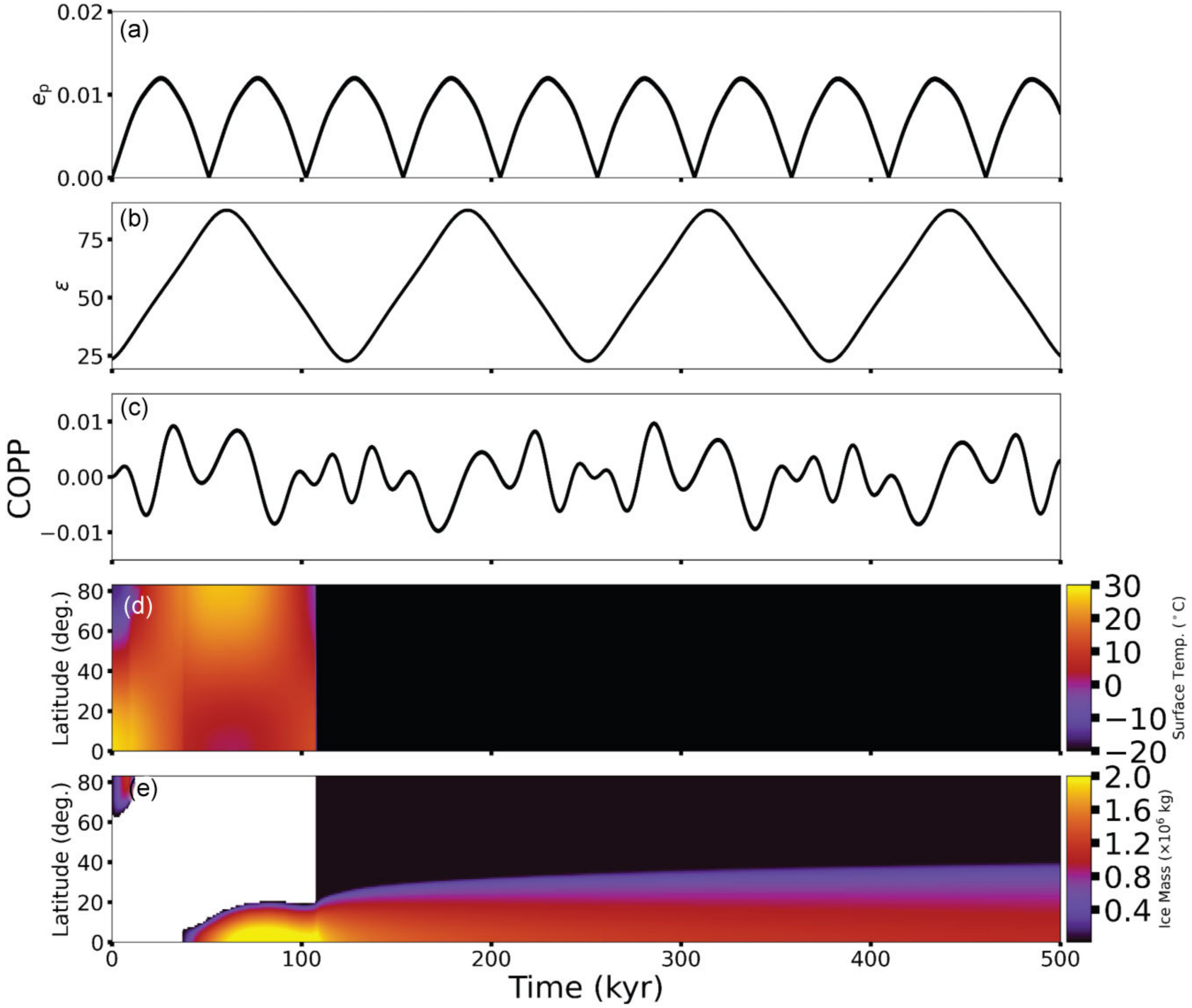

Figure 15. Similar to Fig. 13, but the binary semimajor axis is 30 AU.

Quarles et al. (2019) explored the effect of varying binary orbits on the obliquity variation using an Earth-analogue inclined by 10° orbiting the more massive star of an α Centauri-like binary, where we perform a similar investigation but the planet orbits the less massive star (Fig. 16). We find similar trends, where the variations are shifted towards smaller binary semimajor axis $a_{\rm bin}$ due to a difference in the secular forcing frequency (Andrade-Ines et al. 2016; Quarles et al. 2019). A majority of parameters for the binary orbit permit persistent ice caps with mild Milankovitch cycles, but this is partly due to our choice of initial obliquity, and an ice belt could become the most common if our simulations started the Earth-analogue with a higher obliquity. For $a_{\rm bin} \sim 22$–36 AU, Milankovitch cycles can be dramatic due to switching between states. At the location of the spin-orbit resonance, the Earth-analogue enters a snowball state because ice caps form before the previous phase of an ice belt fully ablates. With significant ice coverage at both the equator and poles, the ice-albedo feedback quickly drives the planet into a snowball state. This is consistent with the snowball instability discussed by Deitrick et al. (2018b) for an Earth-analogue in a dynamically hot multiple planet system orbiting a Sun-like star.

Forgan (2016) used a one-dimensional EBM similar to `POISE`, where the main differences are the heat capacity C is parametrized instead of the albedo α and the orbital/spin evolution is more self-consistently coupled with the climate model. One of the main conclusions of both their work and ours is that Milankovitch cycles for planets in binaries are influenced by the secular forcing of the binary, where Forgan (2016) deduced this through a frequency analysis of the global surface temperature evolution. This work goes beyond this prior analysis in many ways, specifically in the growth/retreat of ice and global distribution of ice. Moreover, we examine a larger variation in the initial planetary spin state, planetary orbit, and binary orbit, where variations in these parameters can dramatically influence the Milankovitch cycles of the Earth-analogue.

As the planetary orbital inclination relative to the binary orbit increases, so does the planet's obliquity variation due to nodal precession. This can lead to more persistent ice caps, an ice belt, or even snowball states, but the first two of these do not necessarily diminish the habitability of the Earth-analogue. Ramirez & Levi (2018) and Paradise et al. (2019) showed for both water worlds and for an Earth-like land/ocean fraction, respectively, that an increased

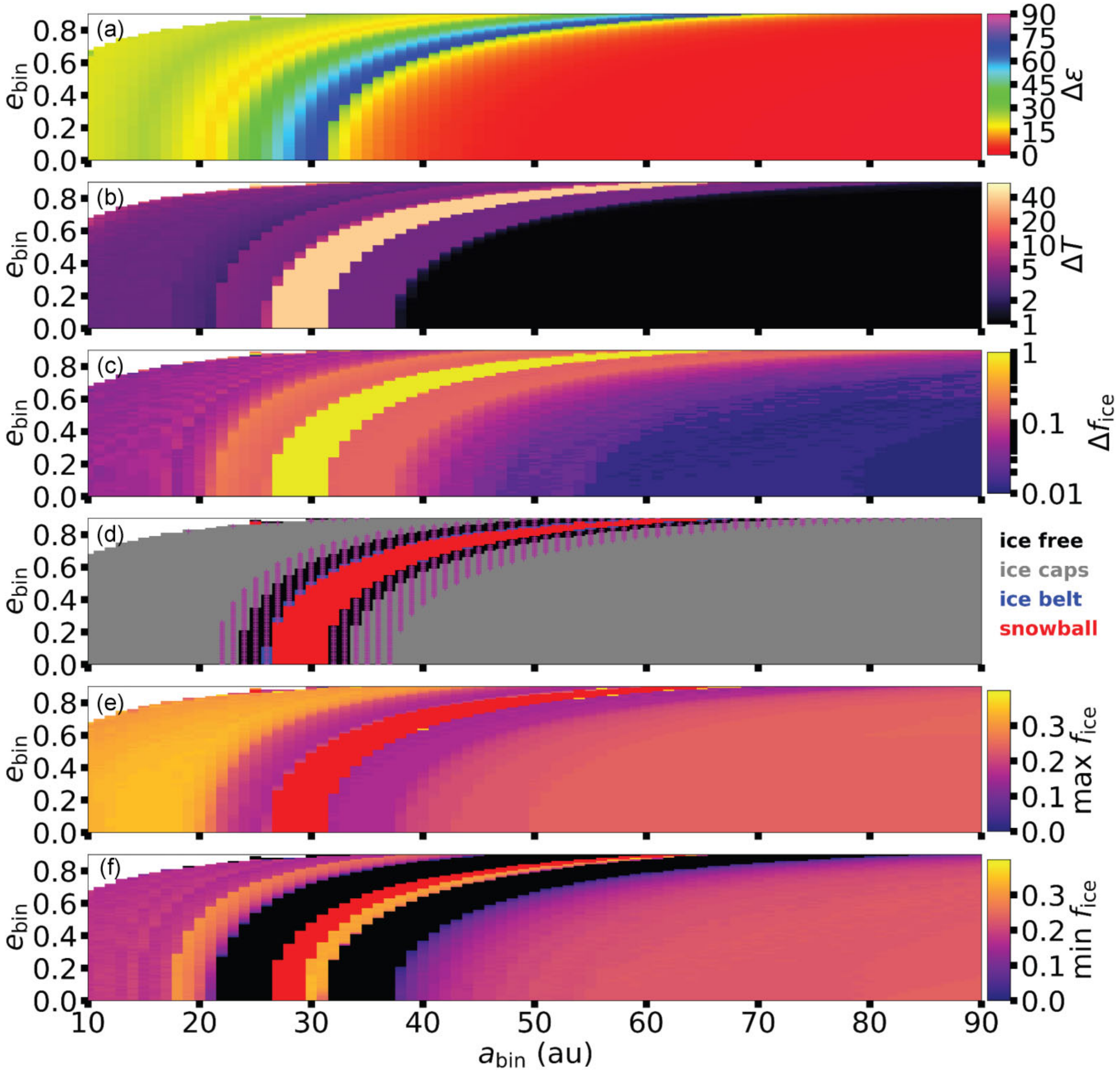

Figure 16. Results of simulations for an Earth-analogue orbiting the secondary star of an α Centauri-like binary, where the binary semimajor axis $a_{\rm bin}$ and eccentricity $e_{\rm bin}$ are varied. The (panel a) obliquity, (panel b) global surface temperature, and (panel c) global ice fraction variations illustrate general structures that impact the potential habitability of the planet. The (panel d) ice distribution state, (panel e) maximum ice fraction, and (panel f) minimum ice fraction show how the binary orbit affects the potential Milankovitch cycles. The white cells (top left-hand panel) indicate orbital parameters, where the planetary orbit would not be stable (Quarles et al. 2020b). The magenta hatched region plotted in panel (d) represents the cases where the planet oscillates between two or three ice distribution states.

CO_2 partial pressure or weathering can allow for some surfaces to be locally ice-free. Haqq-Misra et al. (2019) showed for circumbinary planets the latitudinal surface temperature can increase with different assumptions on the assumed planet topography and land/ocean fraction, where we expect similar effects are possible for eccentric circumstellar planets in binaries. `POISE` has additional options to set the CO_2 partial pressure, change the constants for the outgoing longwave radiation, and mimic Hadley heat diffusion, where varying any one of these could be an interesting avenue for future work. `VPLanet` has an open-source framework, allowing developers to introduce more sophisticated components to `POISE` or even new modules that go beyond the built-in assumptions (Barnes et al. 2020).

Identifying the existence of ice on exoplanets is a future endeavor for next-generation telescopes that have yet to see first light (e.g. LUVOIR; The LUVOIR Team 2019, or HabEx; Gaudi et al. 2020), where albedo variations with respect to the planetary rotation and orbit could provide some of the necessary initial parameters (Schwartz et al. 2016). Further atmospheric characterization with *JWST* (Gardner et al. 2006) would likely be necessary in trying to distinguish between the reflectivity of ice or clouds. For α Centauri AB, the initial step of planet detection has been elusive, but Beichman et al. (2020) proposed a path forward using *JWST* and others in recent years are attempting to detect planets orbiting either star using data taken from ground-based facilities (Trigilio et al. 2018; Zhao et al. 2018; Kasper et al. 2019; Akeson et al. 2021; Wagner et al. 2021).

ACKNOWLEDGEMENTS

This research was supported in part through research cyberinfrastructure resources and services provided by the Partnership for an Advanced Computing Environment (PACE) at the Georgia Institute of Technology. The authors thank Rory Barnes for his guidance in using and modifying `VPLanet` as well as constructive comments that enabled us to improve the quality and clarity of this paper.

DATA AVAILABILITY

Processed data and PYTHON scripts to reproduce the figures are available through the GitHub repository: github.com/saturnaxis/Ice-ages-in-AlphaCen. The raw data from `VPLanet` underlying this paper will be shared on reasonable request to the corresponding author.

REFERENCES

Akeson R., Beichman C., Kervella P., Fomalont E., Benedict G. F., 2021, AJ, 162, 14

Andrade-Ines E., Beaugé C., Michtchenko T., Robutel P., 2016, Celest. Mech. Dyn. Astron., 124, 405

Armstrong J. C., Barnes R., Domagal-Goldman S., Breiner J., Quinn T. R., Meadows V. S., 2014, Astrobiology, 14, 277

Barnes J. W., Quarles B., Lissauer J. J., Chambers J., Hedman M. M., 2016, Astrobiology, 16, 487

Barnes R. et al., 2020, PASP, 132, 024502

Bazsó Á., Pilat-Lohinger E., Eggl S., Funk B., Bancelin D., Rau G., 2017, MNRAS, 466, 1555

Beichman C. et al., 2020, PASP, 132, 015002

Berger A. L., 1978, J. Atmos. Sci., 35, 2362

Brouwer D., Clemence G. M., 1961, Methods of Celestial Mechanics. Academic Press, New York

Bryson S. et al., 2021, AJ, 161, 32

Budyko M. I., 1969, Tellus, 21, 611

Colombo G., 1966, AJ, 71, 891

Cukier W., Kopparapu R. k., Kane S. R., Welsh W., Wolf E., Kostov V., Haqq-Misra J., 2019, PASP, 131, 124402

Deitrick R., Barnes R., Quinn T. R., Armstrong J., Charnay B., Wilhelm C., 2018a, AJ, 155, 60

Deitrick R. et al., 2018b, AJ, 155, 266

Eggl S., Pilat-Lohinger E., Georgakarakos N., Gyergyovits M., Funk B., 2012, ApJ, 752, 74

Eggl S., Georgakarakos N., Pilat-Lohinger E., 2020, Galaxies, 8, 65

Forgan D., 2012, MNRAS, 422, 1241

Forgan D., 2016, MNRAS, 463, 2768

Gardner J. P. et al., 2006, Space Sci. Rev., 123, 485

Gaudi B. S. et al., 2020, preprint (arXiv:2001.06683)

Haghighipour N., Kaltenegger L., 2013, ApJ, 777, 166

Haqq-Misra J., Wolf E. T., Welsh W. F., Kopparapu R. K., Kostov V., Kane S. R., 2019, J. Geophys. Res., 124, 3231

Holman M. J., Wiegert P. A., 1999, AJ, 117, 621

Kaltenegger L., Haghighipour N., 2013, ApJ, 777, 165

Kasper M. et al., 2019, The Messenger, 178, 5

Kasting J. F., Whitmire D. P., Reynolds R. T., 1993, Icarus, 101, 108

Kilic C., Lunkeit F., Raible C. C., Stocker T. F., 2018, ApJ, 864, 106

Kopparapu R. K. et al., 2013a, ApJ, 765, 131

Kopparapu R. K. et al., 2013b, ApJ, 770, 82

Kopparapu R. K., Ramirez R. M., SchottelKotte J., Kasting J. F., Domagal-Goldman S., Eymet V., 2014, ApJ, 787, L29

Kreyche S. M., Barnes J. W., Quarles B. L., Lissauer J. J., Chambers J. E., Hedman M. M., 2020, Planet. Sci. J., 1, 8

Laskar J., Joutel F., Boudin F., 1993, A&A, 270, 522

Lissauer J. J., Barnes J. W., Chambers J. E., 2012, Icarus, 217, 77

Martin R. G., Lissauer J. J., Quarles B., 2020, MNRAS, 496, 2436

Milankovitch M., 1941, Kanon der Erdbestrahlung und seine Anwendung auf das Eiszeitenproblem. Royal Serbian Academy, Belgrade

Moe M., Di Stefano R., 2017, ApJS, 230, 15

Neron de Surgy O., Laskar J., 1997, A&A, 318, 975

North G. R., Coakley J. A., 1979, J. Atmos. Sci., 36, 1189

Paradise A., Menou K., Valencia D., Lee C., 2019, J. Geophys. Res., 124, 2087

Peale S. J., 1969, AJ, 74, 483

Pourbaix D., Boffin H. M. J., 2016, A&A, 586, A90

Quarles B., Lissauer J. J., 2016, AJ, 151, 111

Quarles B., Lissauer J. J., 2018, AJ, 155, 130

Quarles B., Lissauer J. J., Kaib N., 2018, AJ, 155, 64

Quarles B., Li G., Lissauer J. J., 2019, ApJ, 886, 56

Quarles B., Barnes J. W., Lissauer J. J., Chambers J., 2020a, Astrobiology, 20, 73

Quarles B., Li G., Kostov V., Haghighipour N., 2020b, AJ, 159, 80

Raghavan D. et al., 2010, ApJS, 190, 1

Ramirez R. M., Levi A., 2018, MNRAS, 477, 4627

Rein H., Liu S.-F., 2012, A&A, 537, A128

Rein H., Spiegel D. S., 2015, MNRAS, 446, 1424

Rose B. E. J., Cronin T. W., Bitz C. M., 2017, ApJ, 846, 28

Saillenfest M., Laskar J., Boué G., 2019, A&A, 623, A4

Schwartz J. C., Sekowski C., Haggard H. M., Pallé E., Cowan N. B., 2016, MNRAS, 457, 926

Sellers W. D., 1969, J. Appl. Meteorol. Climatol., 8, 392

Shan Y., Li G., 2018, AJ, 155, 237

Shields A. L., Meadows V. S., Bitz C. M., Pierrehumbert R. T., Joshi M. M., Robinson T. D., 2013, Astrobiology, 13, 715

Silsbee K., Rafikov R. R., 2021, A&A, 652, A104

Spiegel D. S., Raymond S. N., Dressing C. D., Scharf C. A., Mitchell J. L., 2010, ApJ, 721, 1308

The LUVOIR Team, 2019, preprint (arXiv:1912.06219)

Trigilio C. et al., 2018, MNRAS, 481, 217

Virtanen P. et al., 2020, Nat. Methods, 17, 261

Wagner K. et al., 2021, Nat. Commun., 12, 922

Ward W. R., Hamilton D. P., 2004, AJ, 128, 2501

Way M. J., Georgakarakos N., 2017, ApJ, 835, L1

Wiegert P. A., Holman M. J., 1997, AJ, 113, 1445

Wilhelm C., Barnes R., Deitrick R., Mellman R., 2021, AJ

Williams D. M., Pollard D., 2003, Int. J. Astrobiol., 2, 1

Zhao L., Fischer D. A., Brewer J., Giguere M., Rojas-Ayala B., 2018, AJ, 155, 24

This paper has been typeset from a TEX/LATEX file prepared by the author.